Recent advances in lanthanide-based nanoparticle contrast agents for magnetic resonance imaging

Synthesis, characterization, and applications

Rahmani, Azmi Aulia; Jia, Qi; Bahti, Husein H.; Fauzia, Retna Putri; Wyantuti, Santhy

DOI
10.1016/j.onano.2024.100226

Publication date
2025

Document Version
Final published version

Published in
OpenNano

OpenNano 21 (2025) 100226

Contents lists available at ScienceDirect

OpenNano

journal homepage: www.elsevier.com/locate/onano

Recent advances in lanthanide-based nanoparticle contrast agents for magnetic resonance imaging: Synthesis, characterization, and applications

Azmi Aulia Rahmani [a], Qi Jia [c], Husein H. Bahti [a,b], Retna Putri Fauzia [a,b,*], Santhy Wyantuti [a,*]

[a] Department of Chemistry, Faculty of Mathematics and Natural Sciences, Universitas Padjadjaran, Jl. Raya Bandung-Sumedang Km. 21 Jatinangor, Sumedang, 45363, Indonesia
[b] Central Laboratory, Universitas Padjadjaran, Jl. Raya Bandung-Sumedang Km. 21 Jatinangor, Sumedang, 45363, Indonesia
[c] Department of Biotechnology, Faculty of Applied Sciences, Delft University of Technology, Van Der Maasweg 9, 2629 HZ, Delft, the Netherlands

ARTICLE INFO

Keywords:
MRI
Contrast agent
Lanthanide nanoparticles

ABSTRACT

MRI is a powerful, non-invasive imaging technique with exceptional soft tissue contrast, requiring contrast agents to enhance sensitivity by shortening longitudinal (T_1) and transverse (T_2) relaxation times. While most clinical agents are chelate-based, their potential toxicity has driven the development of nanoparticle-based alternatives. Nanoparticles offer reduced toxicity, improved stability, prolonged circulation time, and better control over surface properties. Lanthanide-based nanoparticles, in particular, are promising due to their paramagnetic properties enhancing MRI contrast. The design of these nanoparticles focuses on optimizing size, shape, and colloidal stability with advances in synthesis techniques allowing for precise control over particle size, morphology, and stability to significantly influence relaxivity. Larger sizes increase r_2 values but may reduce stability, while anisotropic shapes enhance relaxivity compared to the more stable spheres. Surface modifications with functional polymers improve stability and prevent aggregation, optimizing imaging performance. As research progresses, lanthanide-based nanoparticles are poised to become crucial tools in radiology-driven cancer diagnosis and therapy, offering dual functionality for early detection, targeted treatment, and minimized off-target effects. However, these nanoparticles must be refined for tumour-specific diagnostic and therapeutic applications and undergo comprehensive safety evaluations before clinical trials.

1. Introduction

Medical imaging is important for the early detection, diagnosis, treatment and monitoring of diseases. The most common imaging techniques include computed tomography (CT), X-ray, positron emission tomography (PET), ultrasound (US), single positron emission computed tomography (SPECT), and magnetic resonance imaging (MRI), with MRI being the superior technique due to its non-invasiveness, excellent soft tissue contrast display, high spatial resolution, and absence of ionizing radiation. The low radiation used in MRI sets it apart from invasive imaging methods such as CT and PET, making MRI a safer and more effective option in medical

* Corresponding authors.
E-mail addresses: retna.fauzia@unpad.ac.id (R.P. Fauzia), santhy.wyantuti@unpad.ac.id (S. Wyantuti).

https://doi.org/10.1016/j.onano.2024.100226
Received 6 November 2024; Received in revised form 1 December 2024; Accepted 11 December 2024
Available online 12 December 2024

imaging [1–6].

Given the relatively lower sensitivity of MRI, optimizing its performance involves a strategic application of contrast compounds to expedite relaxation time, consequently refining the image quality. T_1 is a positive contrast agent that accelerates longitudinal relaxation, thereby augmenting brightness in the targeted area, whereas the negative contrast agent T_2 accelerates transverse relaxation, resulting in subdued brightness in the surrounding region. Paramagnetic ion complexes such as gadolinium (Gd^{3+}), manganese (Mn^{2+}), and superparamagnetic iron oxides (SPIONS), are pivotal contrast agents in MRI incorporated into coordination complexes with chelating agents to effectively mitigate the potential toxicity of free metal ions [7–9]. However, gadolinium chelates have several limitations, notably their abbreviated half-life, imprecise distribution, and potential toxicity [10–12].

Nanomaterials have garnered considerable attention for their unique capacity to modulate particle properties within specific biological contexts. Surface modifications of nanoparticles enable tailored adjustments, enhancing in vivo stability (e.g., pegylation to evade macrophage capture) and facilitating targeted delivery to specific organs or tissues (e.g., utilizing overexpressed receptors in diseased regions). Moreover, the customization of nanomaterial sizes serves distinct functional roles: particles below 200 nm preferentially accumulate in cancer cells, those under 15 nm traverse the blood-brain barrier, and sub-6 nm or biodegradable particles can be used for specialized applications. They are also promising inherently superior contrast agents as their nanostructure not only mitigates the risk of toxic metal release but also affords precise control over contrast material distribution while extending the agents' half-life. This pioneering approach holds significant potential for elevating contrast efficiency and potentially reducing dosages [11, 12]. The emergence of nanoscale particles with exceptional properties has significantly propelled advancements in nanomedicine [13]. Lanthanide-based nanoparticles feature 4f unpaired electrons and can serve as contrast agents by accelerating the relaxation of adjacent protons, thereby enhancing MRI imaging contrast. Notably, elements like Tb, Ho, and Dy possess the largest magnetic moments, inducing significant transverse relaxation in hydrogen protons within free water, thus lanthanide-based nanoparticles such as Tb, Ho, and Dy are the optimal choice for ultra-high field T_2 MRI applications [4,14–17].

The use of lanthanide-based nanoparticles as MRI contrast agents requires careful consideration of critical factors such as size, shape, and surface properties, which significantly influence their stability, biocompatibility, and ability to enhance image quality, including contrast resolution (Fig. 1). Understanding these factors is crucial for predicting their behaviour in biological systems and optimizing their application in medical imaging. Surface modifications, such as PEG, TEG, or ligands like folic acid and hyaluronic acid, are employed to improve nanoparticle efficacy, prolong their bloodstream half-life, and enhance their functional properties [2,7]. This review focuses on the synthesis, characterization, and applications of lanthanide nanoparticles in MRI imaging, providing a comprehensive understanding of their potential benefits and challenges as contrast agents.

2. Magnetic resonance imaging (MRI)

During MRI, protons in the body align with an external magnetic field, creating longitudinal magnetization. A targeted radio frequency pulse induces a shift to transverse magnetization, and upon cessation, both magnetization forms return to their original states, emitting radio frequency signals that are captured to create MRI images [18]. The MRI signal depends on the proton density, T_1 (spin-lattice relaxation time), T_2 (spin-spin relaxation time), and proton motion. T_1 represents the time for 63 % of excited protons to realign with the magnetic field, while T_2 is the time for 37 % of proton magnetization to decay in the transverse plane [2,3,19,20]. These relaxation times influence MRI image formation. MRI scanners typically use magnetic fields between 1.5 and 3 T for humans, and 4.7 to 7 T for small animals, with specialized scanners reaching up to 20 T in research settings [21].

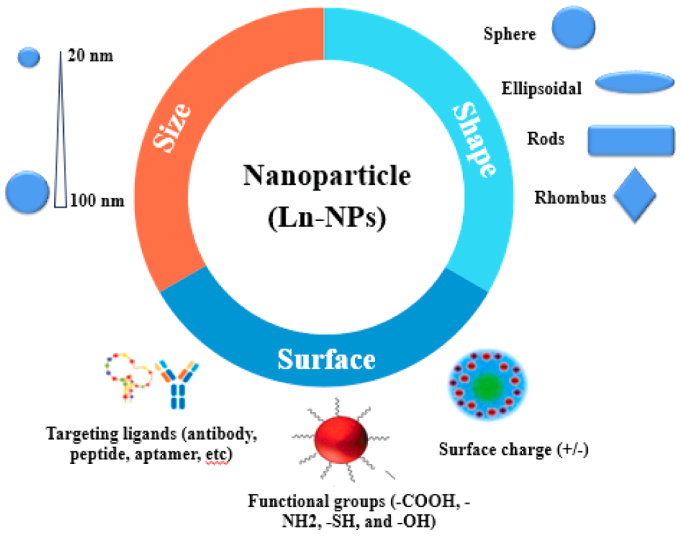

Fig. 1. The application of nanoparticles as MRI contrast agents.

2.1. MRI contrast agent

MRI offers superior spatial resolution in the micrometre range compared to millimetre-based radio diagnostic techniques but it is limited by its low sensitivity, therefore a relatively high local concentration of contrast agent of ~10^{-5} M is necessary to achieve the desired contrast enhancement, In contrast, other imaging methods such as PET, SPECT (with sensitivities ranging from 10^{-11} to 10^{-12} M), and optical fluorescence imaging (with even greater sensitivities from 10^{-15} to 10^{-17} M) are more suitable for detecting and visualizing molecular events at lower concentrations [22,23]. Although MRI can produce highly detailed images, differentiating between similar or adjacent tissue types remains challenging and the resolution relies on contrast agents that accelerate the relaxation time of water protons, either longitudinally (T_1) or transversely (T_2). Since the late 1980s, over 30 % of medical MRI scans have utilized contrast agents to boost the sensitivity and clarity of anatomical images [24]. T_1 contrast agents amplify the T_1 signal on T_1-weighted imaging, yielding positive/bright contrast enhancement, whereas T_2 contrast agents diminish the T_2 signal on T_2-weighted imaging, resulting in negative/dark contrast enhancement [21,25]. Common MRI contrast agents encompass paramagnetic ion complexes such as gadolinium $Gd^{3+}$and manganese Mn^{2+}(T_1) [26–28], as well as superparamagnetic iron oxide nanoparticles (SPION) (T_2) [18,25,29,30].

Lanthanide oxide nanoparticles, such as Dy^{3+}, Ho^{3+}, and Tb^{3+}, are effective MRI contrast agents due to their high paramagnetic moments at room temperature which are sufficient to induce spin relaxation of water protons. The magnetic moment is derived from the spin-orbital motion of the 4f electrons, which are shielded by the 5 s and 5p orbitals, thereby mitigating the influence of surface effects. This enhances their suitability as MRI contrast compounds, particularly in high magnetic resonance fields. Additionally, since the rapid motion of the 4f electrons does not correspond to the slower spin motion of water protons, these nanoparticles primarily affect T_2 relaxation, resulting in efficient negative contrast in MRI images while exerting minimal impact on T_1 relaxation [31–33].

3. Synthesized of lanthanide nanoparticles

Various methodologies have been employed to synthesize lanthanide nanoparticles with wet chemical methods emerging as the preferred techniques for synthesizing nanoparticles suitable for biomedical applications. These methods, relying on precipitation reactions, necessitate meticulous control over ion release, requiring precise adjustments in synthesis parameters such as reagent concentrations, temperature, solvent choice, and the incorporation of specific additives [34]. Controlled ion release is achieved by the hydrolysis or thermal decomposition of precursors, with additives forming ion complexes acting as both capping and dispersing agents.

The commonly used hydrothermal method uses water as a solvent [35] and is performed in an autoclave, with the process controlled by adjusting the temperature and/or pressure (Fig. 2). The temperature is increased beyond the boiling point of water to vapour saturation and the selection of raw materials, acidity (pH), time, and temperature controls the crystal size, morphology, and degree of agglomeration [36,37]. Typically, a rare earth precursor solution is mixed with the precipitation agent such as HNO_3 [38], NaOH [39,40] or urea [41] before being placed in a Teflon autoclave and heated to above 150 °C for 6–24 h [36]. Wu et al. [42] successfully synthesized nanoparticles by combining hyaluronic acid with Gd_2O_3 nanoparticles. The incorporation of hyaluronic acid, a tumour-targeting agent [43], increased biocompatibility, enhanced tumour targeting, and reduced side effects.

The following reactions occur during the hydrothermal synthesis of nanoparticles [31,33]:

Acidification: Ln_2O_3 (bulk) + $6HNO_3 \rightarrow 2\ Ln(NO_3)_3 + 3H_2O$, (1)

Hydrolysis: $Ln(NO_3)_3 + 3NaOH \rightarrow Ln(OH)_3 + 3NaNO_3$, (2)

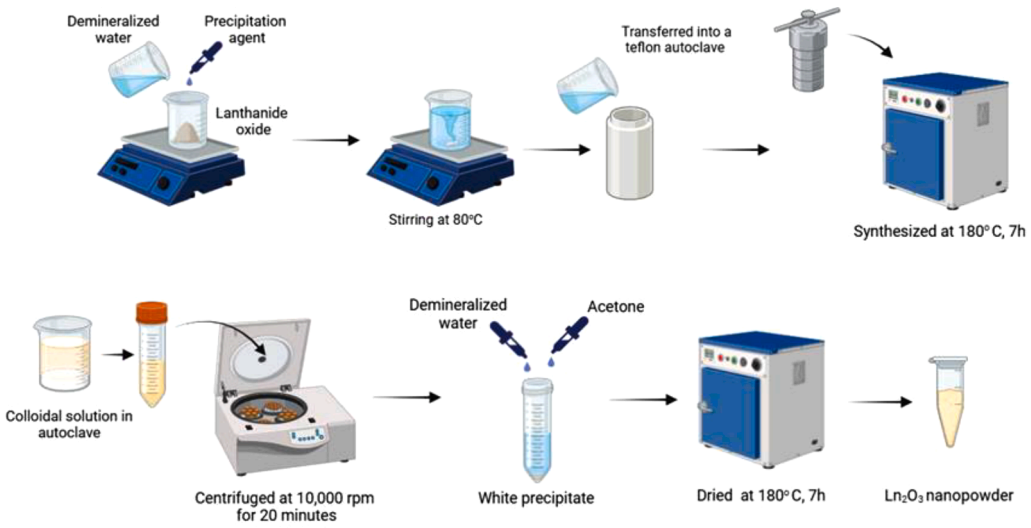

Fig. 2. The synthesis of Ln_2O_3 via the hydrothermal method.

Dehydration: $2Ln(OH)_3 \rightarrow Ln_2O_3$ (nanopowder) + $3H_2O$. (3)

The solvothermal method has also emerged as a promising approach for the fabrication of well-crystallized and biocompatible lanthanide-based magnetic particles due to its ability to provide controlled reaction conditions. This technique facilitates the precise tuning of particle size, morphology, and crystalline structure. Additionally, it is a simple single-step procedure conducted at relatively low temperatures, making it cost-effective and easy to scale for larger production [44,45]. Solvothermal and hydrothermal methods utilize high pressure and temperature in a closed system but differ in the type of solvent used. Hydrothermal uses water, making it environmentally friendly and suitable for aqueous-based material synthesis, whereas solvothermal employs organic solvents like ethylene glycol, allowing solvent control and producing materials with unique characteristics. Since some solvents are toxic, polymer coatings, such as polyethylene glycol (PEG), have been used to enhance biocompatibility and control the particle size, thereby increasing their stability and effectiveness in biomedical applications.

Zang et al. [46] synthesized Ho_2O_3 nanoparticles using the solvothermal method with ethylene glycol as the solvent and PEG-4000 as the capping agent for 10 h at 200 °C. Similarly, Dougherty et al. [45] synthesized Gd_2O_3 nanoparticles employing ethylene glycol as the solvent and PEG-4000 as the capping agent for varying durations (3, 5, and 8 h) at 180 °C to evaluate the effect of reaction time on the particle properties.

The utilization of the polyol method is prevalent in biomedical applications due to the uniform size (average diameter of ±2.0 nm) and shaped nanoparticles produced which can be surface coated with hydrophilic ligands, all accomplished in one pot synthesis process [1,7,12,43,47] as shown in Fig. 3.

The highly adaptable nanoparticle surface facilitates efficient molecular binding through diverse interactions. However, surface modification using hydrophilic materials is required to make the nanoparticles non-toxic and biocompatible for interactions with cells [48–51]. Polymers with abundant hydrophilic binding groups are superior surface coatings compared to small molecules, facilitating effective interactions. For example, polyacrylic acid (PAA), polymethyl vinyl ether-alt-maleic acid (PMVEMA), polyacrylic acid-co-maleic acid (PAAMA), polyaspartic acid (PASA), and D-glucuronic acid with multiple COOH groups [1,7,12,43,47,52]. In addition, the nanoparticle surface can be conjugated with cancer-targeting ligands, such as folic acid (FA) and/or cyclic arginylglycylaspartic acid (cRGD) [53].

Lanthanide-based nanoparticles can also be synthesised by thermal decomposition. Cai et al. [52] transformed gadolinium nanoplates using the positively charged polymer polyethyleneimine (PEI) before modifying these functionalized nanoplates with PEG chains to create PEI-PEG complexes (Fig. 4). The encapsulated Gd_2O_3 biocompatible clusters that coated the Gd_2O_3 nanoplates enabledT_1-weighted MRI [52].

Each nanoparticle synthesis method offers unique advantages and limitations based on the reaction conditions, scalability, and biocompatibility. An overview of the key features and differences, highlighting their advantages and disadvantages, is summarized in Table 1 to aid in selecting the most suitable approach for specific applications, particularly in biomedicine. The hydrothermal and solvothermal methods rely on high-pressure systems, with the former using water as a solvent for eco-friendly synthesis and the latter employing organic solvents for enhanced control over particle properties. The polyol method stands out for producing highly uniform and small nanoparticles, while the thermal decomposition method excels in generating monodisperse particles with precise functionalization.

The selection of ligands for surface coating is also critically important to enhance stability, biocompatibility, and interactions with the biological environment, significantly impacting the effectiveness of nanoparticles in biomedical applications. This includes their ability to internalize within cells and their excretion. Moreover, the nanoparticle size and shape impact their biomedical application. Smaller nanoparticles generally exhibit a higher surface area-to-volume ratio, potentially increasing their relaxivity due to enhanced interactions with water molecules. Additionally, the shape of nanoparticles affects their magnetic properties, influencing their ability to induce changes in relaxation levels (r_1 or r_2), thereby impacting their effectiveness as MRI contrast agents. Certain shapes can enable more efficient interactions with the magnetic field, further influencing the relaxation [2,31,54].

4. Characterization of lanthanide nanoparticles

4.1. Size and shape

Lanthanide nanoparticles synthesized via the one-pot polyol method display an exceptionally small, uniform shape, which is critical for optimal performance in imaging applications. High-resolution transmission electron microscopy (HRTEM) indicates that D-glucuronic acid-coated Ln_2O_3 nanoparticles (Ln = Tb, Dy, and Ho) have a consistent average size of approximately 2 nm. Additionally, these nanoparticles exhibit excellent dispersion within aqueous media, remain stable without sedimentation for over a week and can be readily redispersed with gentle agitation if settling occurs, demonstrating their suitability for use in biomedical environments [7].

Marasini et al. [32] employed high-resolution transmission electron microscopy (HRTEM) to estimate the diameter of PAA surface-coated lanthanide synthesized via a one-pot polyol method as shown in Fig. 5c (Tb) and Fig. 5d (Ho). The core of the nanoparticles was visible through the lattice lines in the HRTEM images, while the PAA coating surrounding the core was not visible due to the small polymer size. The nanoparticles were ultrasmall and nearly spherical with an estimated average diameter of 1.8 ± 0.1 nm for Tb_2O_3 nanoparticles and 1.7 ± 0.1 nm for Ho_2O_3 nanoparticles. As shown in Fig. 5a and Fig. 5b, the colloidal stability of the nanoparticles was well maintained in the medium without precipitation for 20 days, which is consistent with the minimal interaction of PAA with proteins such as albumin at physiological pH. Laser light scattering (Tyndall effect) observed in the nanoparticle suspension indicated good colloidal dispersibility in aqueous solution [32].

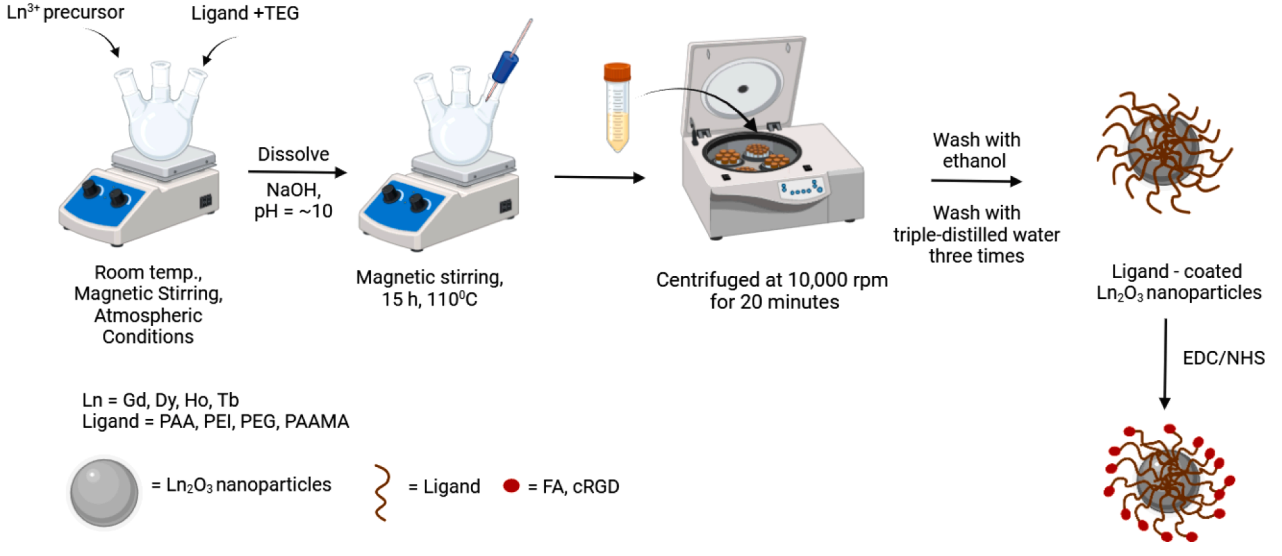

Fig. 3. The polyol method to synthesize lanthanide nanoparticles. TEG = triethlene glycol (Adapted from groups [1,7,12,43,47]).

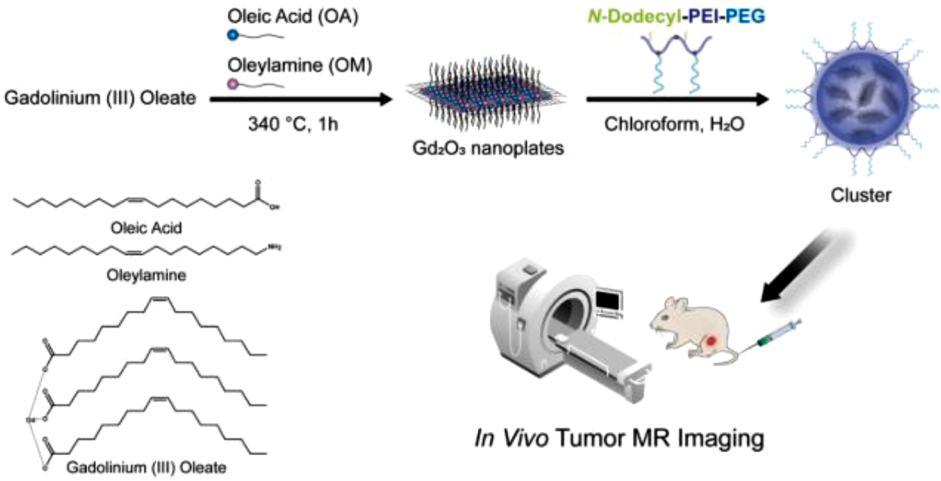

Fig. 4. Synthesis of Gd_2O_3@N-dodecyl-PEI-PEG clusters by thermal decomposition (Reprinted with permission from [52] Copyright © 2019, Elsevier).

Guleria et al. [55] synthesized gadolinium oxide nanoparticles by the polyol method using different chain length glycols as a capping agent including diethylene glycol (DEG), triethylene glycol (TEG), tetraethylene glycol (TeEG), and polyethylene glycol (PEG 200) (Fig. 6). The Gd_2O_3 nanoparticles were spherical and agglomerated with an average diameter of 13 ± 2 nm, 16 ± 2 nm, 19 ± 3 nm and 21 ± 2 nm, respectively. The particle size increased with increasing glycol chain length with shorter glycol chains with larger hydroxyl groups being more effective capping agents, producing smaller nanoparticles [55].

Gomez et al. synthesized uniform $NaDy(MoO_4)_2$ nanoparticles intended as MRI contrast agents with a particular focus on high-field applications. Through precise control of experimental conditions, the researchers achieved defined nanoparticle shapes and sizes, key determinants of their magnetic relaxivity and overall performance. The spherical $NaDy(MoO_4)_2$ NPs had an average diameter of 23 nm (Fig. 7a), while the ellipsoidal variants had mean lengths of 50 (Fig. 7b), 68 (Fig. 7c), and 87 (Fig. 7d) nm. This variability enabled the exploration of how size and shape influence relaxivity rates (r_1 and r_2) which are critical for contrast efficacy in MRI. The study emphasizes the potential to refine nanoparticle morphology to enhance imaging quality by aligning particle properties with specific MRI magnetic field requirements [54].

Dougherty et al. [45] synthesized PEG-coated $Gd(CO_3)_3$ nanoparticles using a solvothermal method with $Gd_2(CO_3)_3$ as the precursor and PEG as the surfactant. The SEM characterization in Fig. 8a–c reveals particle agglomeration of $Gd_2(CO_3)_3$ in the form of rhomboidal shards, with the particle size increasing as the heating time was extended. Fig. 6d showing calcination at 400 °C presents molten material indicating that PEG was not fully released from the Gd_2O_3 product, whereas uniform spherical nanoparticles with an average size of 80 nm were formed at calcination at 800 °C (Fig. 8e), demonstrating that high-temperature calcination yielded more uniform stable nanoparticles.

Predominantly spherical gadolinium nanoparticles were synthesized using the hydrothermal method [38] as shown in Fig. 9a, although some degree of aggregation was observed due to the presence of relatively larger particles. This accumulation is likely due to the high molecular weight of PEG, as the long PEG chains contain numerous hydrogen bonds that promote interactions between particles leading to clumping. The size distribution of the spherical nanoparticles ranged from 46.9 to 141 nm, with most nanoparticles falling within the 40−60 nm range. The EDX spectrum in Fig. 9b shows distinct peaks corresponding to gadolinium (Gd) and oxygen (O), confirming their presence in the nanoparticles. The weight percentages were determined to be 56.077 % for Gd and 43.923 % for O, while the atomic percentages were 11.496 % for Gd and 88.504 % for O, further confirming the composition of the synthesized Gd_2O_3 nanoparticles [38].

X-ray diffraction (XRD) analysis was utilized to determine the crystal structure of the nanoparticles. The broad peaks indicated their amorphous nature, attributed to their exceedingly small particle diameter. However, subsequent examination of the XRD pattern after TGA (thermogravimetric analysis) revealed well-defined peaks, signifying the crystallization of the nanoparticles after heat treatment to 900 °C [7]. Examples of the XRD patterns of PAA-coated ultrafine Dy_2O_3 nanoparticles and ultra-small Gd_2O_3 nanoparticles with PMVEMA before and after TGA are shown in Fig. 10. Notably, peaks corresponding to the (222), (400), (440), and (622) planes of the highly crystallized cubic structure of lanthanide nanoparticles were observed [56]. The peak shown in the diffraction corresponds to the Joint Committee on Powder Diffraction Standard (JCPDS) 43–1014 [45].

PEG-Ho_2O_3 nanoparticles were synthesized and extensively validated through a combination of characterization techniques [57]. As illustrated in Fig. 11a, the XRD pattern displayed diffraction peaks at (222), (400), (440), and (622) corresponding to the standard cubic Ho_2O_3 phase (Ia3) as outlined in JCPDS no. 43–1018. This confirmed that the nanoparticles adopted the cubic crystal structure characteristic of Ho_2O_3. Importantly, no additional peaks corresponding to impurities or secondary phases were observed, indicating the high purity of the synthesized nanoparticles and confirming that the calcination process effectively preserved the desired phase.

Table 1
A summary of the methods to synthesize lanthanide-based nanoparticles.

Synthesis Method	Solvent	Reaction Conditions	Advantages	Disadvantages
Hydrothermal	Water	High temperature (>150 °C) and pressure in an autoclave for 6–24 h	Enables control over size, morphology, and agglomeration Environmentally friendly because water is used as the solvent	Extended reaction time
Solvothermal	Organic solvents (e.g., ethylene glycol)	Moderate temperature (e.g., 200 °C) and pressure in a closed system	Better control of crystallinity and morphology Cost-effective and scalable	Toxicity of some organic solvents
Polyol	Polyols (e.g., Triethylene glycol)	Elevated temperatures (160–200 °C)	Produces uniform nanoparticles One-pot synthesis	Produces small-diameter nanoparticles
Thermal decomposition	Organic solvents or metal-organic precursors (e.g., oleic acid)	High temperatures for decomposition of metal-organic precursors	Produces highly crystalline nanoparticles. Precise control over properties	Toxicity Soluble in organic solvents

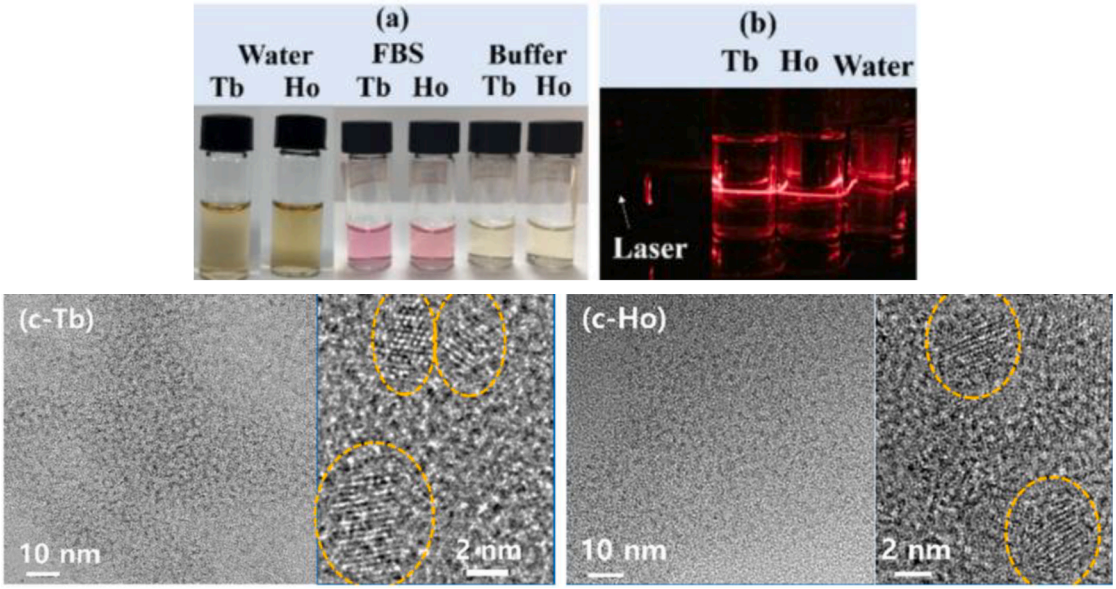

Fig. 5. (a) Nanoparticle suspensions in aqueous media, including 10 % FBS in RPMI1640 medium and sodium acetate buffer solution (pH = 7.0), (b) laser light scatter effect (i.e., Tyndall effect) evidencing nanoparticle dispersion., HRTEM images (c) Tb_2O_3 and (d) Ho_2O_3 nanoparticles (Reprinted with permission from [32] Copyright © 2021 by Marasini et al., MDPI).

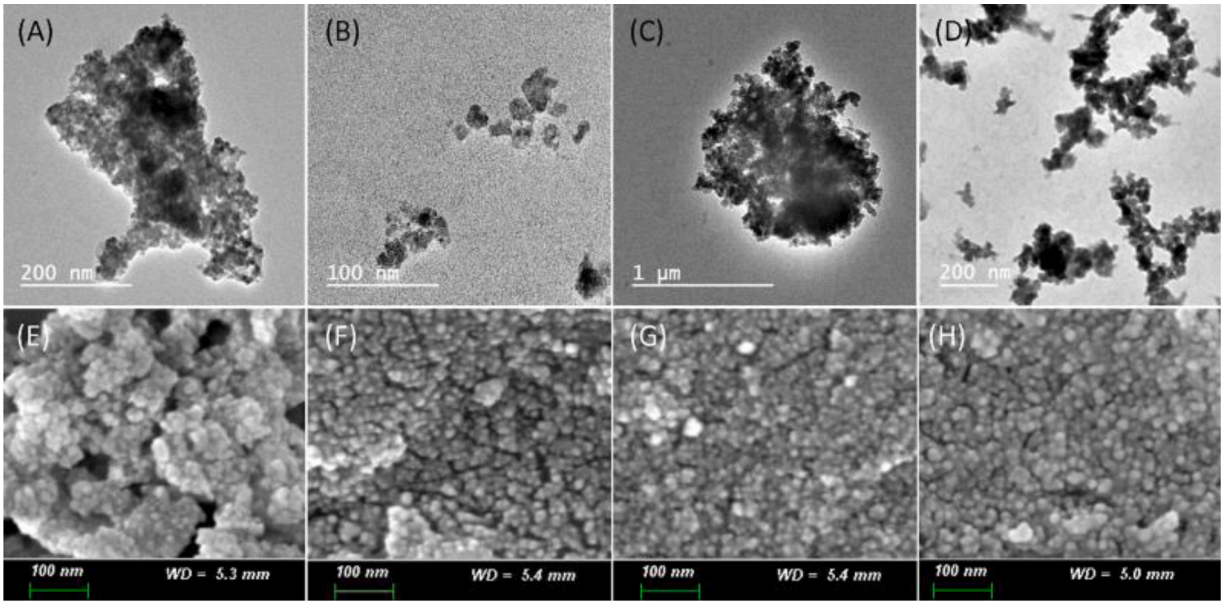

Fig. 6. (A-D) TEM and (E-H) SEM imagesfor DEG-Gd_2O_3, TEG-Gd_2O_3, TeEG-Gd_2O_3, and PEG-Gd_2O_3 (Reprinted with permission from [55] Copyright © 2019 American Chemical Society).

Furthermore, EDX analysis (Fig. 11b) verified the presence of only two elements, holmium (Ho) and oxygen (O), confirming that no extraneous elements were incorporated during synthesis and that the nanoparticles were composed solely of the intended Ho_2O_3 phase [57].

In addition to the initial structural confirmation, the crystal structure of Ho_2O_3 nanoparticles was analysed by XRD before and after thermal treatment (TGA), as shown in Fig. 12. Before TGA (Fig. 12a), the XRD patterns exhibited broad peaks and amorphous features, indicating a disordered structure attributed to the ultrasmall nanoparticle size which limits the ability of X-rays to detect well-defined crystal arrangements. After thermal treatment at 900 °C, the XRD patterns displayed sharp diffraction peaks, reflecting significant crystal growth and increased particle size (Fig. 12b). These post-TGA diffraction peaks were indexed to the (222), (400), (440), and (622) crystal planes, corresponding to the Miller indices (hkl) of the cubic Ho_2O_3 structure. The lattice constant of the TGA-treated

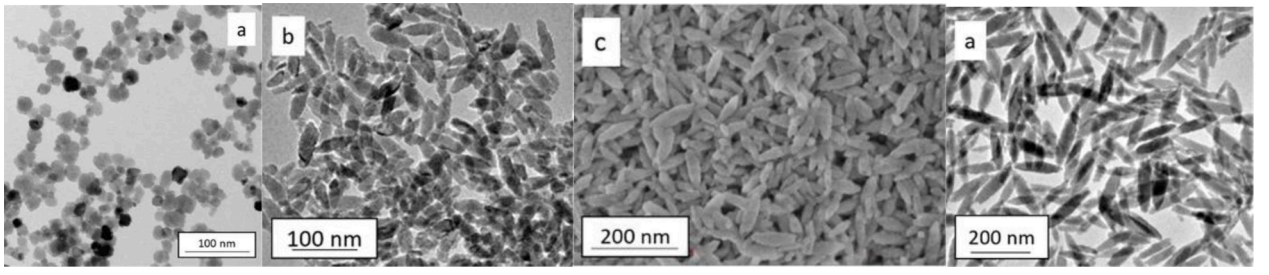

Fig. 7. HRTEM images of Spherical $NaDy(MoO_4)_2$ Nanoparticles (A) 23 nm and ellipsoidal (B) 50 × 16 nm (C) 68 × 20 nm (D) 87 × 22 nm (Reprinted with permission from [54] Copyright © 2022 Elsevier).

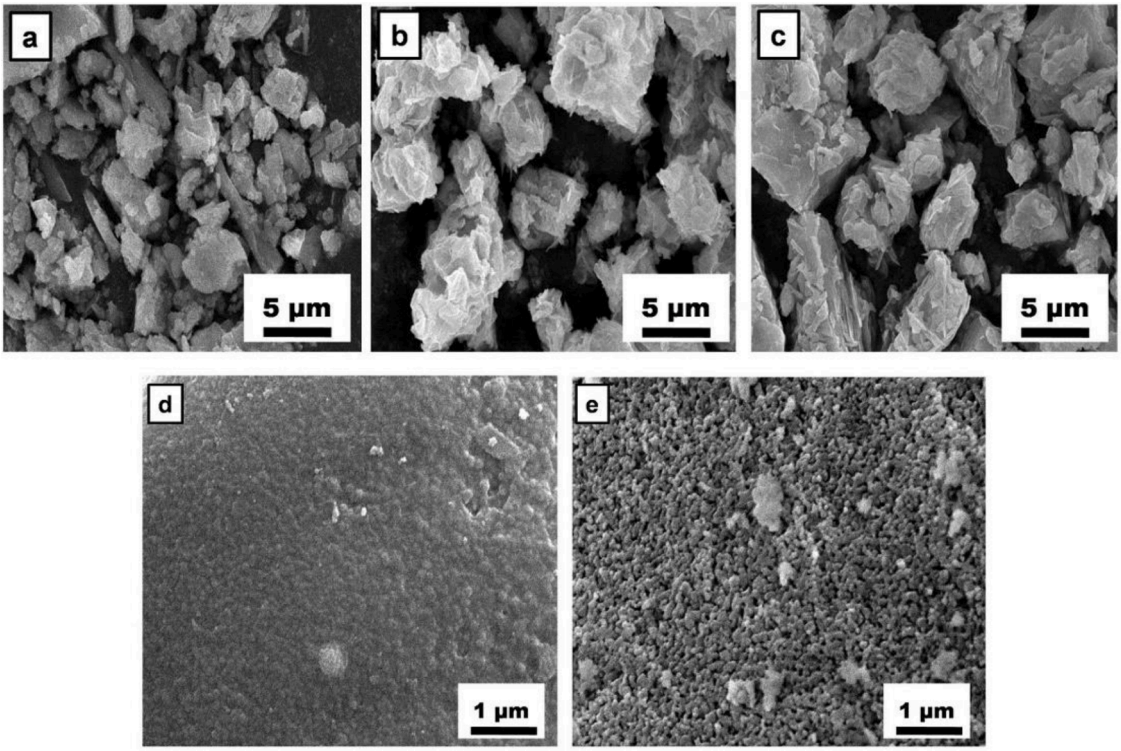

Fig. 8. $Gd_2(CO_3)_3$ particles functionalized with PEG polymer after decomposition for (a) 3 (b) 5 (c) 8 h and Gd_2O_3 nanoparticles after calcination at (d) 400 °C and (e) 800 °C (Reprinted with permission from [45] Copyright © 2018, Elsevier).

samples was 10.607 Å in line with the previously reported value of 10.606 Å based on the JCPDS reference card (Card No. 01-074-1829), demonstrating high accuracy in lattice parameter determination [33].

Furthermore, the structural analysis was extended to $HoPO_4$ nanoparticles, as shown in Fig. 13, where the XRD patterns exclusively displayed reflections corresponding to the tetragonal $HoPO_4$ phase (PDF 01–076–1533) with a flat background. This absence of any other crystalline or amorphous phases indicated the high sample purity. The crystallite sizes were calculated using the Scherrer formula from the reflection peak at approximately 35° 2θ and were 31 nm for Ho27, 52 nm for Ho48, and 85 nm for Ho80 nanoparticles. The similarity between the crystallite size and the particle edge suggests that all three types of nanoparticles exhibit single-crystal characteristics [58].

X-ray photoelectron spectroscopy (XPS) is a surface-sensitive technique that analyses the elemental composition and chemical states of materials by measuring the binding energies of emitted core electrons. It is particularly useful for characterizing nanoparticles and thin films in which their surface properties are critical to their functionality. The synthesis and characterization of Dy_2O_3-based nanoparticles with a carbon coating confirmed the material structure and composition. The XPS spectrum of the DYO@C nanoparticles (Fig. 14) revealed the key elements, carbon (C), oxygen (O), sodium (Na), and dysprosium (Dy), as well as sodium, originating from NaOH during synthesis. The spectrum also indicated the presence of different forms of carbon, including C–H and C–O from polymerized dextrose, and C═C and C═O from the amorphous carbon coating, confirming the nanoparticle surface structure. The observed electron binding energies (EBEs) were consistent with the literature, validating the surface composition of the DYO@C nanoparticles [15].

The core-shell structural composite nanoparticles, specifically PEG salicylic acid-gadolinium (Gal-PEG-2000), synthesized by Zhang et al., [59] are a promising material for biomedical applications due to their functional surface chemistry and biocompatibility. The full XPS spectrum (Fig. 15a) shows characteristic peaks for C 1 s, O 1 s, and Gd 3d at binding energies of 284 eV, 530 eV, and 1223 eV, respectively, confirming their presence on the nanoparticle surface. The Gd 3d fine spectrum (Fig. 15b) exhibited peaks at 1186 eV and 1218 eV corresponding to the energy levels of Gd $3d_{5/2}$ and Gd $3d_{3/2}$, respectively, indicating the presence of gadolinium. The C 1 s fine spectrum revealed three distinct components (Fig. 15c) C–C/C═C (carbon-carbon single or double bonds), C–O (carbon-oxygen single bonds), and C═O (carbon-oxygen double bonds), suggesting diverse carbon bonding configurations derived from the PEG structure. Similarly, the O 1 s fine spectrum was fitted into two bonding structures, O—C (oxygen-carbon single bonds) and O═C (oxygen-carbon double bonds) consistent with the findings for C 1s. Quantitative analysis indicated atomic percentages of 28.31 % for carbon, 71.11 % for oxygen, and 0.07 % for gadolinium. The high oxygen content reflects the dominance of PEG on the nanoparticle surface, as PEG is rich in oxygen-containing functional groups. Overall, the results confirmed that Gal-PEG-2000 nanoparticles are predominantly coated with PEG with minimal gadolinium content, supporting PEG's role in enhancing the stability and biocompatibility of the nanoparticles [59].

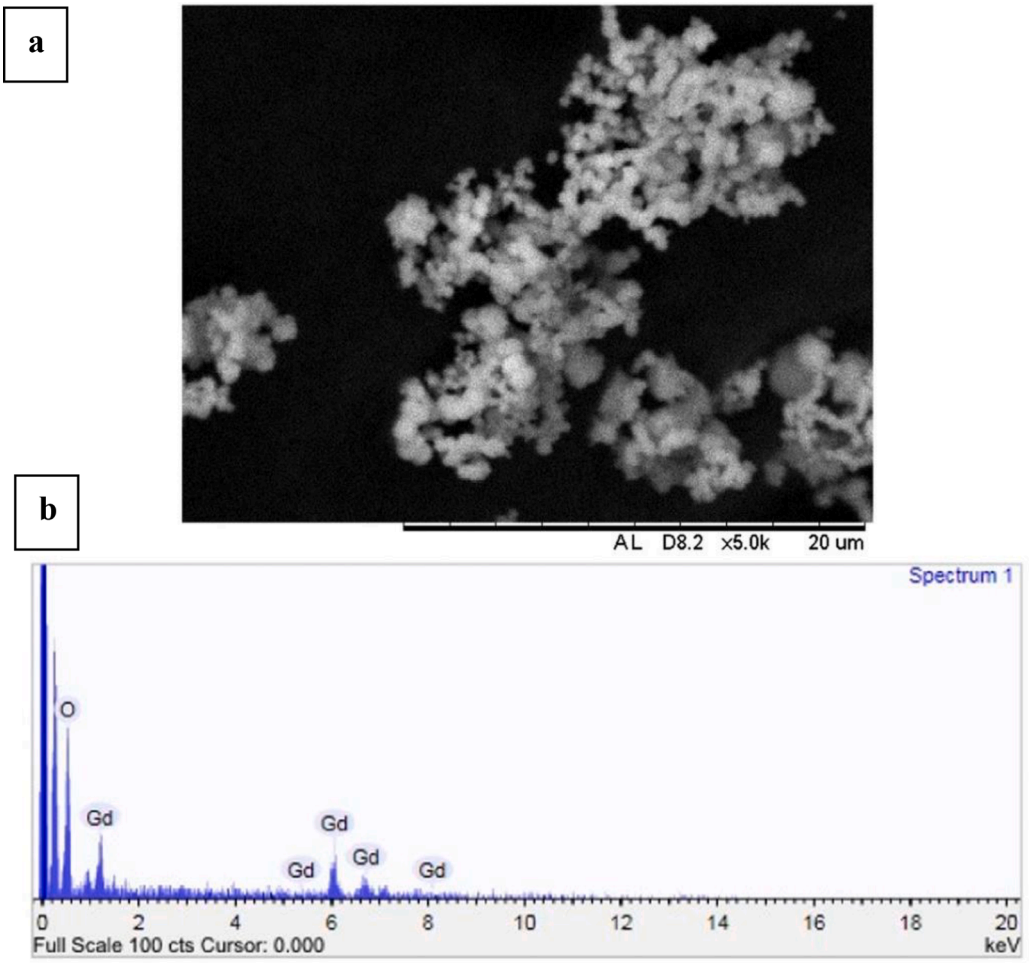

Fig. 9. (a) SEM analysis of Gd nanoparticles at a magnification of 5000x and their corresponding (b) EDX spectrum (Reprinted with permission from [38] Copyright © 2023, Elsevier).

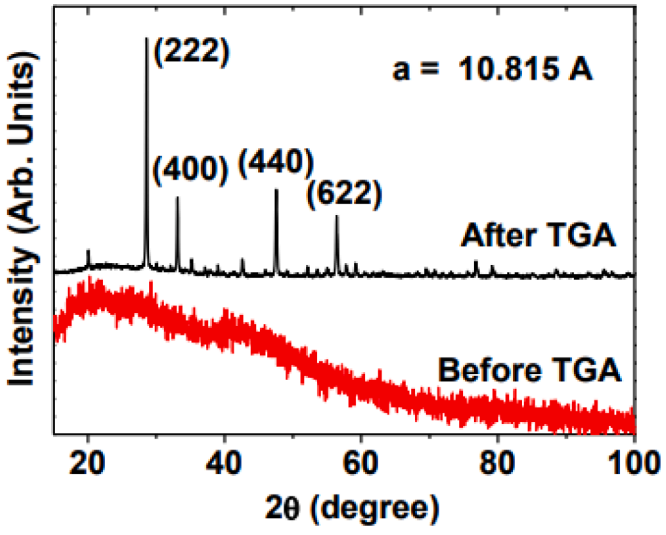

Fig. 10. XRD patterns of the powder sample of PAA-coated ultra-small Gd_2O_3 nanoparticle with PMVEMA before and after TGA (Reprinted with permission from [1] Copyright © 2020 by Ahmad et al., MDPI).

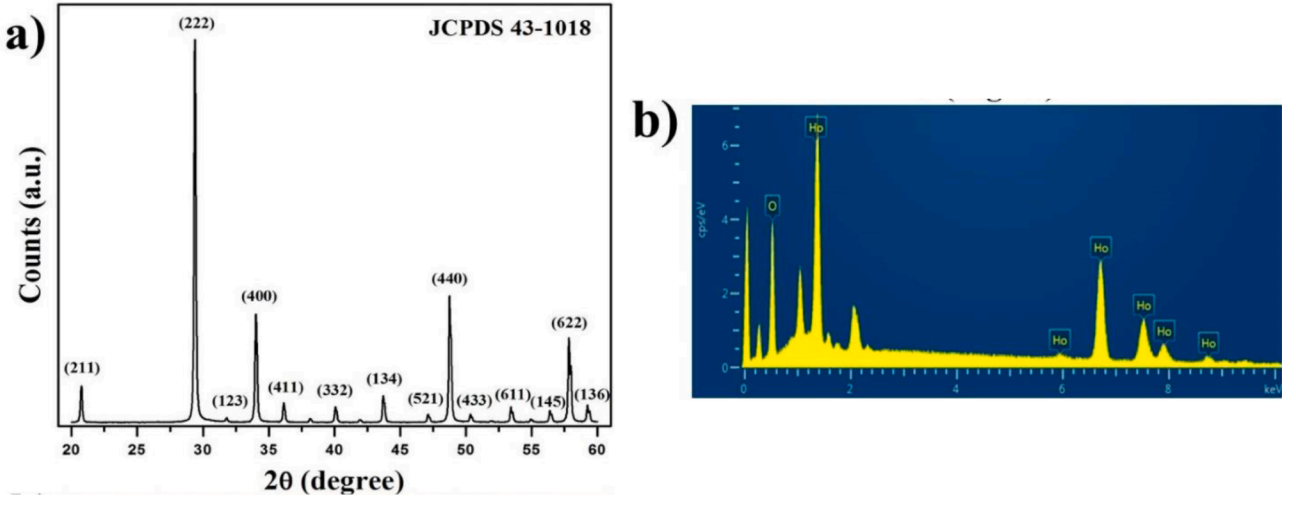

Fig. 11. (a) XRD patterns and (b) EDX analysis of the synthesized Ho_2O_3 nanoparticles (NPs) (Reprinted with permission from [57] Copyright © 2017 by Atabaev et al., MDPI).

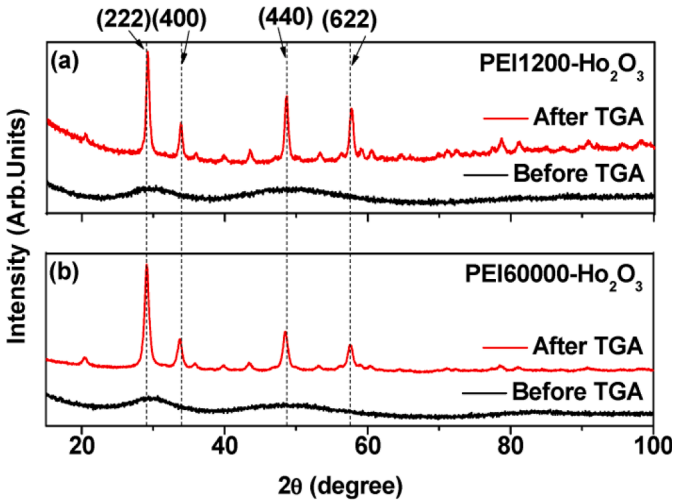

Fig. 12. XRD patterns of the powder sample of (a) PEI1200- and (b) PEI60000-coated ultrasmall Ho_2O_3 nanoparticles before and after TGA (Reprinted with permission from [33] Copyright © 2022 by Liu et al., MDPI).

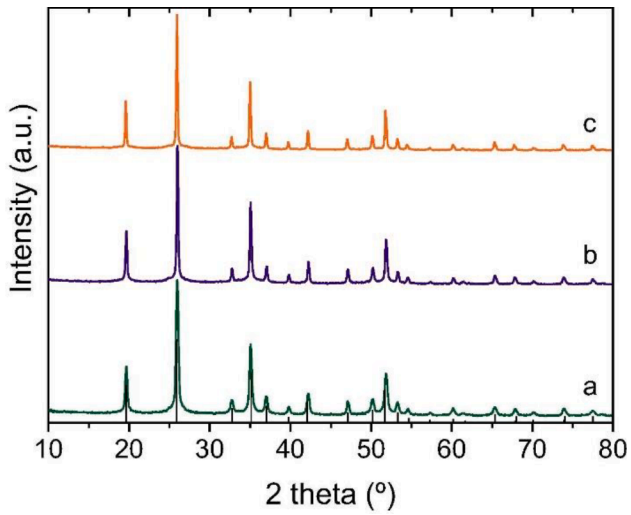

Fig. 13. XRD patterns of Ho27 (a), Ho48 (b), and Ho80 (c) nanoparticles (NPs). The ticks at the bottom of the graph correspond to the tetragonal $HoPO_4$ phase (PDF 01–076–1533) (Reprinted with permission from [58] Copyright © 2020, Elsevier).

4.2. Surface coating

The surface coating of nanoparticles with hydrophilic and biocompatible ligands is essential for their utilization as MRI contrast agents and can be characterized by FTIR analysis. An example of the FTIR spectrum of Gd_2O_3 nanoparticles coated with PMVEMA in Fig. 16 provides compelling evidence regarding the surface coating of Gd_2O_3 NPs with PMVEMA. There were distinctive bands observed including the C—H stretching band at 2942 cm^{-1}, COO^- bands at 1547 cm^{-1} (antisymmetric) and 1404 cm^{-1} (symmetric), and the C—O stretching band at 1079 cm^{-1}. Notably, the COO^- stretching band of PMVEMA separated into symmetrical and anti-symmetrical bands, exhibiting a red shift compared to the C═O stretching band at 1700 cm^{-1} in the free PMVEMA spectrum attributed to the coordination bonding of COO^- to the Gd^{3+} bridge on the NP surface, signifying the establishment of a robust coordination bond between the hard base COO^- of PMVEMA and the hard acid Gd^{3+} on the Gd_2O_3 NP surface. Furthermore, the unconnected COO^- group in PMVEMA appeared as COO^-Na^+ due to synthesis conditions at pH ~10. The significant red shift observed in the COO- stretching band implies the formation of multiple coordination bonds between PMVEMA and the nanoparticle surface, supporting the successful attainment of the intended coating [1,8].

Another example of surface coating on lanthanide nanoparticles is provided in Fig 17, showing that the samples exhibited distinct absorption peaks characteristic of PAA, notably featuring the C–H stretch at 2936 cm^{-1} and the C═O stretch at 1697 cm^{-1} (Fig. 17a). However, the observed C═O stretches indicated a red shift of approximately 154 cm^{-1} compared to free PAA, owing to the

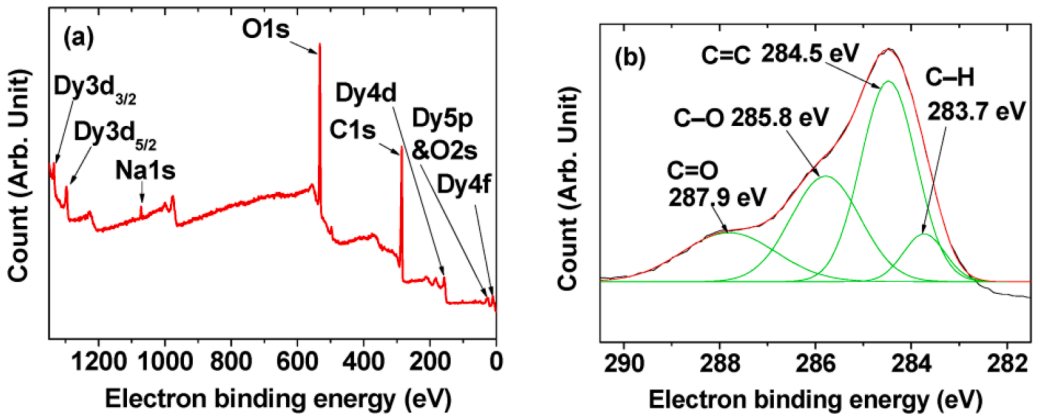

Fig. 14. XPS spectra of DYO@C nanoparticles: (a) Full range scan displaying the presence of C, O, Na, and Dy elements in the nanoparticle sample, and (b) carbon peak revealing four distinct types of carbon (Reprinted with permission from [15] Copyright © 2020 by Yue et al., MDPI).

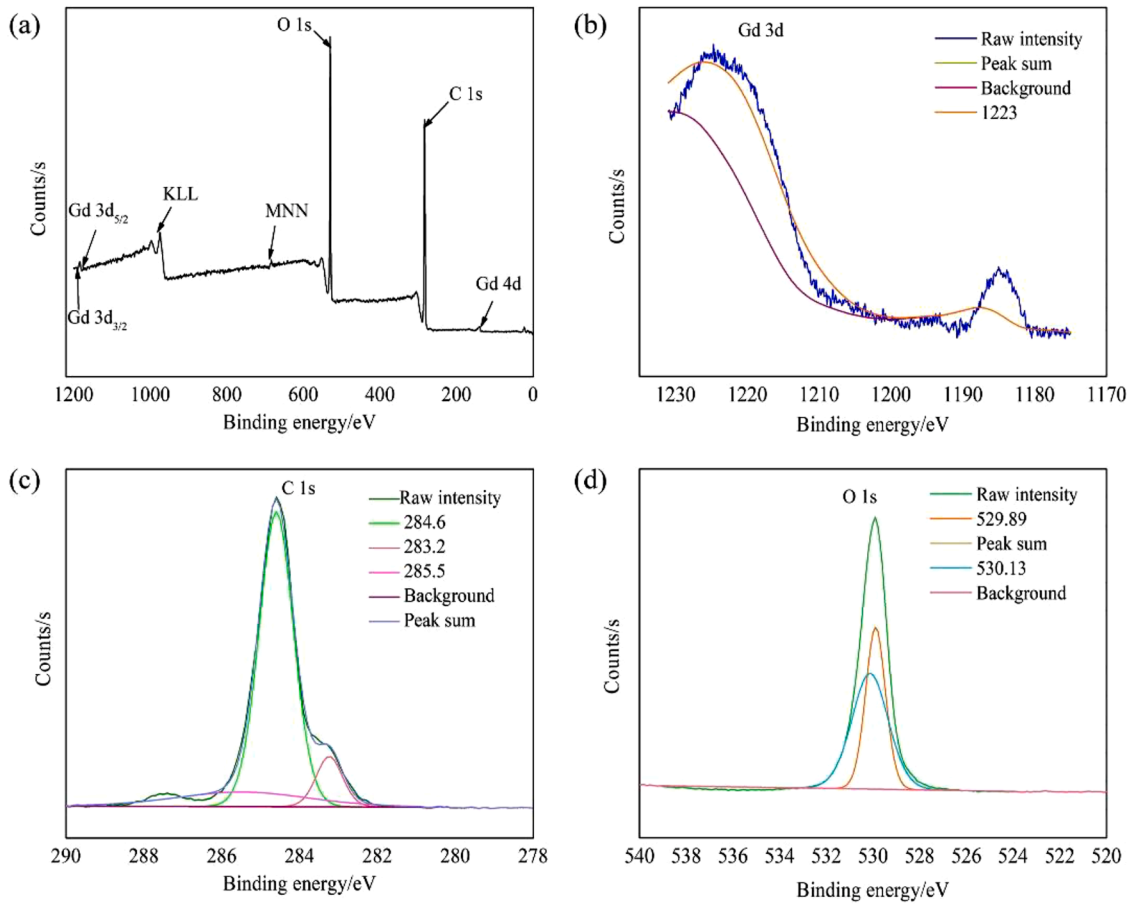

Fig. 15. (a) Wide-scan XPS spectrum of Gal-PEG-2000, (b) Gd 3d, (c) C 1 s, and (d) O 1 s (Reprinted with permission from [59] Copyright © 2021, Elsevier).

electrostatic bonding between the COO^- groups and Ln^{3+} (Ln = Tb, Ho, Dy, Gd) on the nanoparticle surfaces. There were two discernible peaks around 1555–1535 cm^{-1} and 1395–1400 cm^{-1}, denoting the asymmetric and symmetric stretching frequencies of COO^-, respectively. These frequencies signify the bridge-bonding of COO^- with Ln^{3+} on the NP surface, as depicted in Fig. 17b. Considering that each PAA molecule (Mw = ~1800 Da) encompasses approximately 25 carboxylic groups, it is conceivable that multiple groups per PAA were conjugated to each nanoparticle. The free carboxylic groups of PAA in the PAA-coated nanoparticles

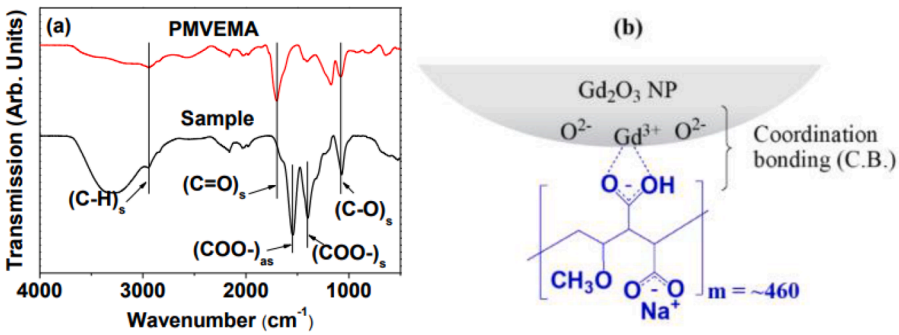

Fig. 16. (a) FTIR absorption spectra and (b) surface-coating structure of Gd_2O_3 coated PMVEMA (Reprinted with permission from [1] Copyright © 2020 by Ahmad et al., MDPI).

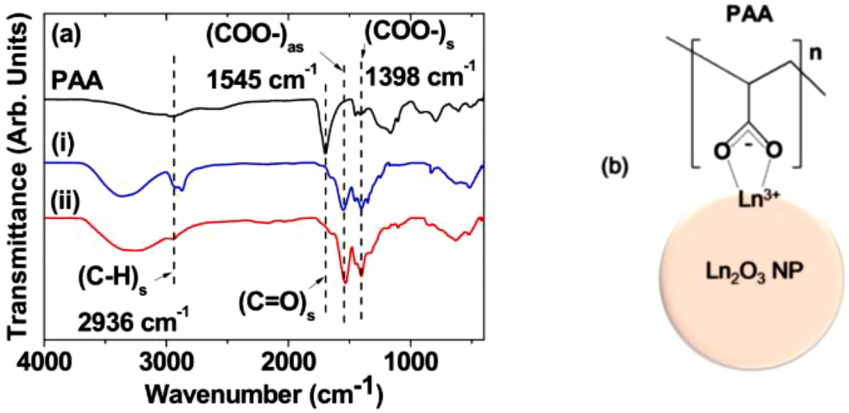

Fig. 17. (a) FTIR absorption spectra and (b) surface-coating structure of Ln_2O_3 coated PAA (Reprinted with permission from [32] Copyright © 2021 by Marasini et al., MDPI).

existed as COO^-Na^+ not COOH using NaOH during synthesis, potentially overlapping with peaks around 1555 cm^{-1}, slightly higher than the conjugated COO^- to Ln^{3+} (= ~1545 cm^{-1}). Hence, discerning the peaks of free carboxylic groups (COO^-Na^+) of PAA in the PAA-coated nanoparticles was challenging due to their similarity to the peaks of COO^- conjugated to Ln^{3+} [8,12].

Other surface modifications of nanoparticles can also be achieved using PEG. Typically, PEG-6000 is used as a stabilizing agent to achieve uniform spherical shape and reduce nanoparticle size by inhibiting particle growth and aggregation. The hydroxyl groups of PEG on the surface of Gd^{3+} provide colloidal stability through van der Waals forces between oxygen in the PEG molecule and positive groups on the Gd^{3+} surface (Fig. 18). As PEG absorbs onto the particle surface, its activity decreases, limiting particle growth. The presence of PEG also controlled colloidal stability through steric repulsion with the increased molecular weight resulting in increased

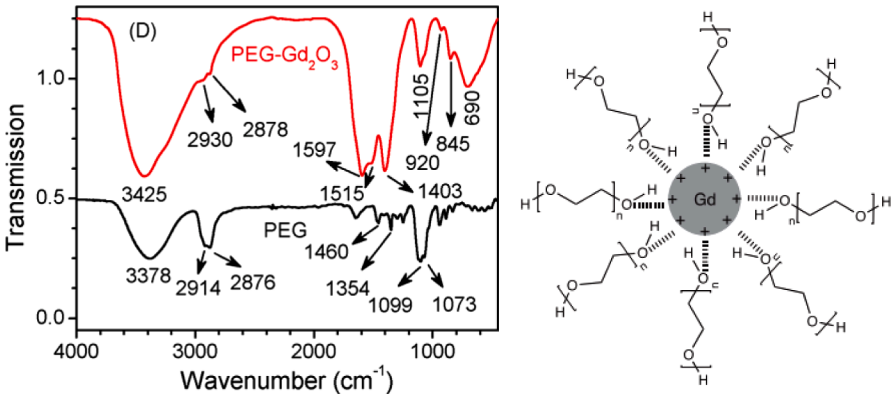

Fig. 18. (a) FTIR absorption spectra (Reprinted with permission from [53] Copyright © 2019 American Chemical Society) and (b) Surface-coating structure of Gd_2O_3 coated PEG (Reprinted with permission from [38] Copyright © 2023, Elsevier).

distance between nanoparticles to prevent aggregation [9,31,51]. The FTIR spectrum of PEG-Gd_2O_3 exhibits several characteristic bands across different wavelengths: O—H stretching vibrations at 3390–3380 cm^{-1}, C—H stretching vibrations at 2930 and 2880 cm-1 from the polymer's methyl groups, along with bands at 1456 and 1350 cm^{-1} attributed to CH_2 bending and fluttering vibrations. Additionally, peaks ranging between 1130 and 1050 cm^{-1} are observed due to C—O and C—O-C stretching vibrations. Upon coating the Gd_2O_3 NPs with PEG, a broad band emerges at 3425–3410 cm^{-1} originating from the O—H stretching vibrations of the surface hydroxyl groups from adsorbed glycol and molecular water. However, the most crucial absorption band lies within the range of 1070–1110 cm^{-1} arising from the stretching of C—O-C and C—O bonds in the -CH_2–O-CH_2- groups of the glycol, a characteristic feature of the polyol confirming the successful coating of nanoparticles [55]. The characteristic peak observed near 690 cm^{-1} corresponds to the Gd-O stretching vibration, indicating the formation of Gd_2O_3 [38,55,60].

The analysis of C—H and C═O stretching in the PAAMA spectra of the powder samples (Fig. 19a) confirms the successful surface coating of Gd_2O_3 nanoparticles with PAAMA. Fig. 19b illustrates the PAAMA coating structure on the nanoparticle surface, revealing robust bonding between multiple carboxylic groups and Gd^{3+} entities. Notably, the COO^- stretch at 1537 cm^{-1} exhibits a pronounced red shift of 161 cm^{-1} from the C═O stretch at 1698 cm^{-1} in free PAAMA, verifying the presence of a strong coordination bond. Such observed red shifts are common in various metal oxide nanoparticles coated with ligands containing carboxylic groups. This bonding pattern aligns with a hard acid (Gd^{3+} on the nanoparticle surface)-hard base (COO^- from PAAMA) coordination interaction [47].

Dy_2O_3-based nanoparticles with a carbon coating were synthesized and characterized using various spectroscopic techniques [15]. The FTIR spectrum (Fig. 20a) revealed two distinct peaks at 1568 and 1384 cm^{-1} corresponding to the G- and D-bands of C=C stretching. These bands, absent in the spectrum of free dextrose, confirm the presence of a carbon coating on the nanoparticle surface. The Dy-O stretching peak at 550 cm^{-1} was observed in both the sample and bare Dy_2O_3 nanoparticles, confirming the presence of Dy_2O_3. Raman spectroscopy (Fig. 20b) verified the G- and D-bands at 1569 and 1412 cm^{-1}, respectively, supporting the nature of the carbon coating. Additionally, the O—H stretching peak at 3240 cm^{-1} confirmed the presence of numerous OH groups on the surface, while peaks at 1065 cm^{-1} (C—O) and 2970 cm^{-1} (C—H) indicated the presence of polymerized dextrose on the nanoparticle surface. TGA was employed to estimate the amounts of carbon coating (59.3 %) and core Dy_2O_3 (32.9 %) nanoparticles (Fig. 20c). Elemental analysis (EA) revealed provided a carbon coating percentage of 63.32 %, consistent with the TGA results. Further evaluation of the carbon coating composition showed that 33.8 % originated from the enhanced carbon content of dextrose, with the remaining 66.2 % from polymerized dextrose. This suggests that the carbon coating is formed by the polymerization of dextrose on the nanoparticle surface, producing amorphous carbon sheets terminated with polymerized dextrose, which imparts stability to the nanoparticles in aqueous solutions.

The nanoparticle surface coating significantly influences the stability, dispersibility, and interactions in various environments. Characterization using dynamic light scattering (DLS) and zeta potential analysis provides critical insights into these properties. DLS measures the hydrodynamic diameter, revealing size distribution and aggregation tendencies, while zeta potential (ζ potential) reflects the strength of electrostatic interactions between dispersed particles measured in millivolts (mV). Changes in these parameters reflect the effectiveness of the surface coating in maintaining nanoparticle stability under different conditions.

Gomez Gonzalez at al. [61] surface-modified $DyVO_4$ nanoparticles using a PAA polymer to enhance the colloidal stability. DLS analysis revealed that the hydrodynamic diameter of $DyVO_4$@PAA nanospheres in a physiological pH simulator (MES) medium (pH 6.5) was 94 nm (Fig. 21d), closely resembling the diameter in water (pH 5.7, Dh = 87 nm; Fig. 21d). Both values were only slightly larger than the average particle size observed from TEM images. PAA forms a hydrophilic layer around the nanoparticles, leading to an increase in the hydrodynamic diameter measured by DLS compared to unmodified nanoparticles. DLS measures the nanoparticle size, including the hydration layer or molecules bound to its surface, rather than just the particle core, therefore, the adsorbed PAA layer contributes to the detected increase in hydrodynamic size. Furthermore, the zeta potential of the $DyVO_4$@PAA colloid increased to +49 mV, whereas it was only −37 mV in the absence of PAA. This increase in surface charge is likely due to the adsorption of PAA molecules onto the nanoparticle surface. PAA contains carboxyl groups (-COOH) that ionize in media with a certain pH generating negative charges that interact with the nanoparticles. In this case, the PAA layer helps prevent nanoparticle aggregation by enhancing electrostatic repulsion between the particles. Additionally, the increase in zeta potential indicates that PAA improves the surface charge of

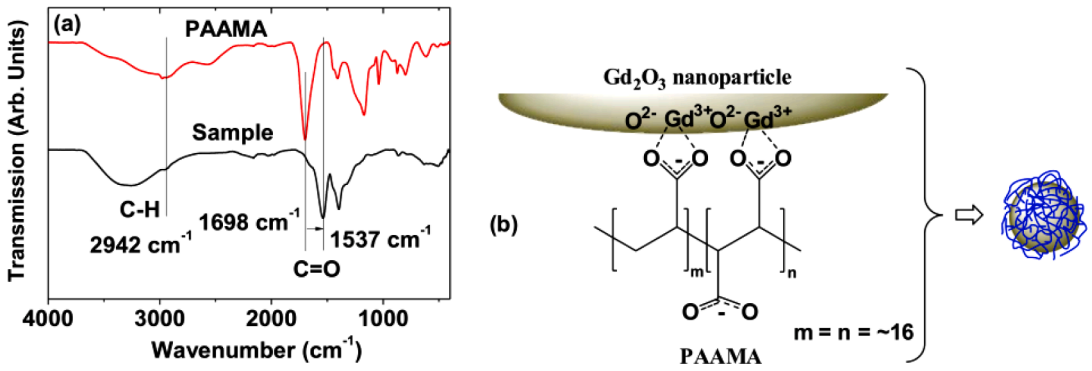

Fig. 19. (a) FTIR absorption spectra and (b) Surface-coating structure of Gd_2O_3 coated PAAMA (Reprinted with permission from [47] Copyright © 2020 by Jang et al., MDPI).

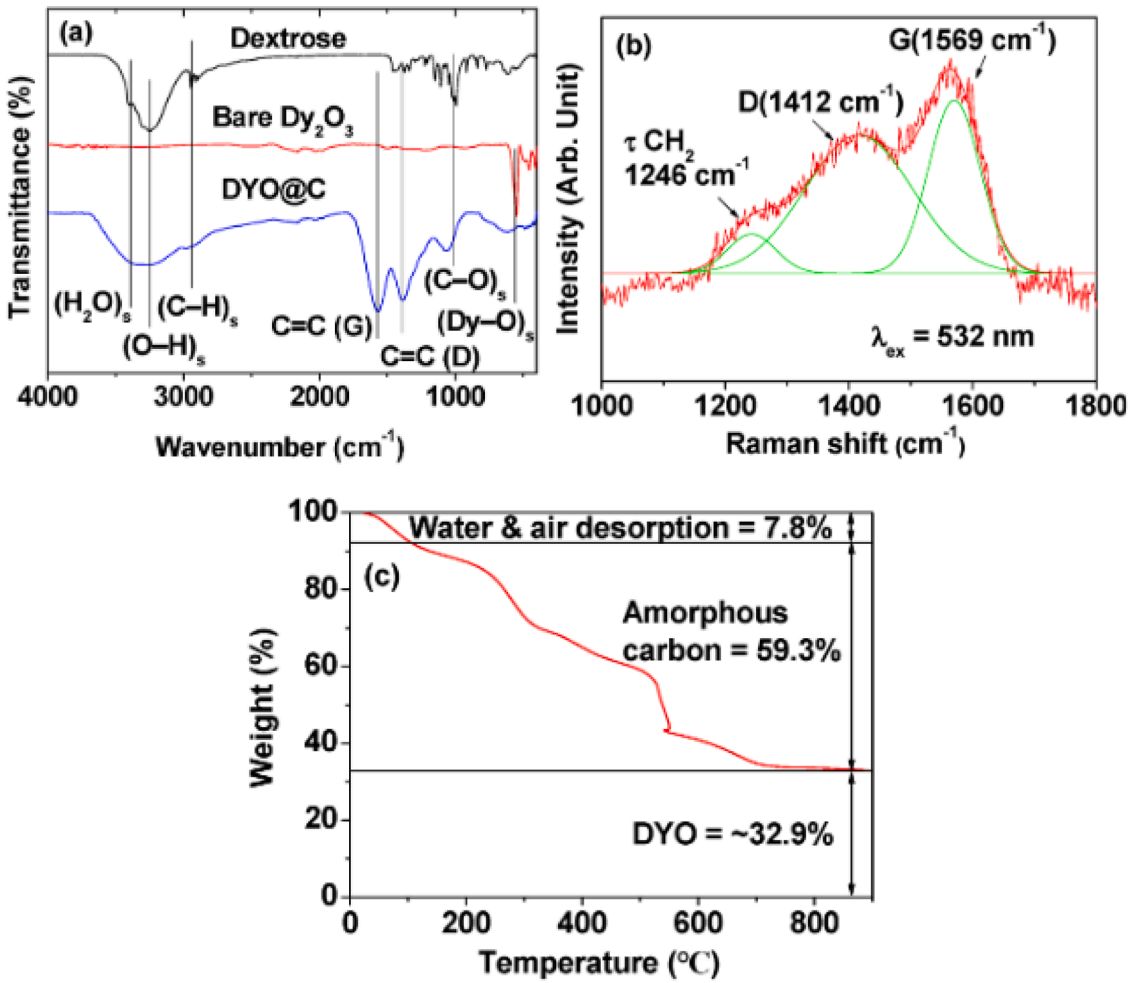

Fig. 20. (a) FTIR absorption spectra of free dextrose, uncoated Dy_2O_3 nanoparticles, and DYO@C nanoparticles; (b) Raman spectrum of the DYO@C nanoparticles (excited with a 532 nm laser wavelength); (c) TGA curve for the DYO@C nanoparticles (Reprinted with permission from [15,47] Copyright © 2020 by Yue et al., MDPI).

the nanoparticles, thereby strengthening the colloidal stability in the solution. Negatively charged nanoparticles exhibit lower interactions with plasma proteins, contributing to their enhanced stability in blood circulation compared to positively charged counterparts. This reduced protein adsorption minimizes opsonisation, a process where proteins tag particles for clearance by the immune system, thereby prolonging their circulation time and improving their potential for effective drug delivery or imaging applications [62].

The surface modification of Gd_2O_3 nanoparticles with N-Dodecyl-PEI-PEG resulted in an average zeta potential of +23.73 mV, attributed to the positive charge on the amine groups of PEI [52]. In comparison, another surface modification using PEG yielded a higher average zeta potential of $+36.7 \pm 0.802$ mV, indicating stronger electrostatic repulsion and enhanced colloidal stability [38]. Generally, a zeta potential value greater than ±30 mV indicates strong electrostatic repulsion between particles effectively preventing agglomeration and ensuring the stability of the colloidal system [63]. The zeta potential is a critical parameter for predicting the stability of nanoparticle dispersions, with high zeta potential values, whether positive or negative, indicating that the particles in the suspension will repel each other, thereby preventing aggregation and maintaining colloidal stability, whereas low zeta potential values lead to particle aggregation, reducing the stability of the suspension [38,64,65].

5. Imaging properties of lanthanide nanoparticle

Relativity is a pivotal parameter in assessing the efficacy of contrast enhancement in MRI contrast agents. Typically, higher relativity levels yield superior contrast enhancement at equivalent dosages or adequate contrast at reduced dosages. Enhanced magnetic relativity, enhancing MRI image contrast, serves as a metric for its efficacy and is quantified as the concentration-normalized increase in longitudinal or transverse relaxation rates ($1/T_1$ or $1/T_2$) per millimole of contrast agent ($mM^{-1}\ s^{-1}$) [4,27,66,67]. The r_1 and r_2 values are influenced by the number of water molecules around the nanoparticles and the distance between them and, therefore,

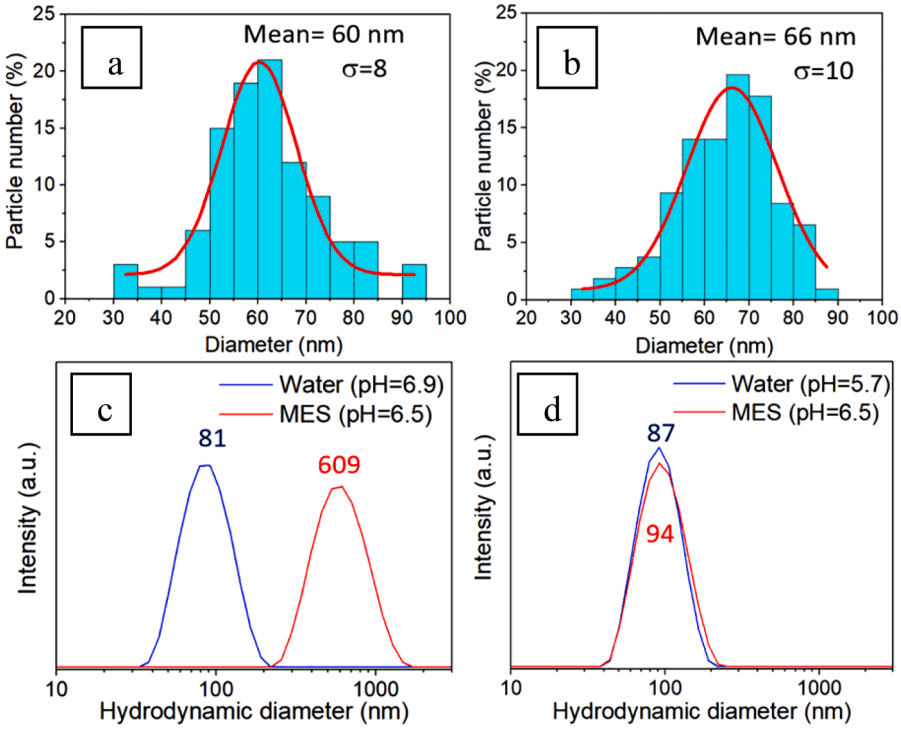

Fig. 21. Particle size histograms of (a) $DyVO_4$ and (b) $DyVO_4$@PAA nanoparticles and hydrodynamic diameter distribution curves of $DyVO_4$ nanoparticles in (c) water and $DyVO_4$@PAA nanoparticles in (d) a physiological pH simulator (MES) (Reprinted with permission from [61] Copyright © 2021 *American Chemical Society*).

depend on the attraction of water to the ligand capabilities around the nanoparticles [68].

5.1. T_1 contrast agents

Gadolinium-based nanoparticles exhibit highly suitable relaxation properties for T_1 MRI contrast agents, primarily attributable to the exceptionally high spin magnetic moment ($s = 7/2$) associated with Gd^{3+}, surpassing that of all other elements within the periodic table [3,26,50,69,70]. Gd_2O_3 nanoparticles possess a larger molecular size/weight, leading to extended retention times and enabling prolonged examinations. Moreover, their increased gadolinium content enhances the device's detection capabilities [71]. In the 3.0 T MR field, the r_1 and r_2 values for PAAMA-coated Gd_2O_3 nanoparticles were 40.6 and 63.4 $mM^{-1}\ s^{-1}$, respectively, utilizing the plots of $1/T_1$ and $1/T_2$ versus the concentration of Gd as shown in Fig. 22a [47]. Amongst various hydrophilic biocompatible polymers characterized by multiple carboxylic groups, namely PAA [8], PASA [72], and PMVEMA [1], the Gd_2O_3 nanoparticles coated with PAAMA stand out due to their comparatively smaller diameter size and notably higher r_1 value. Due to the presence of ~288 COO^-

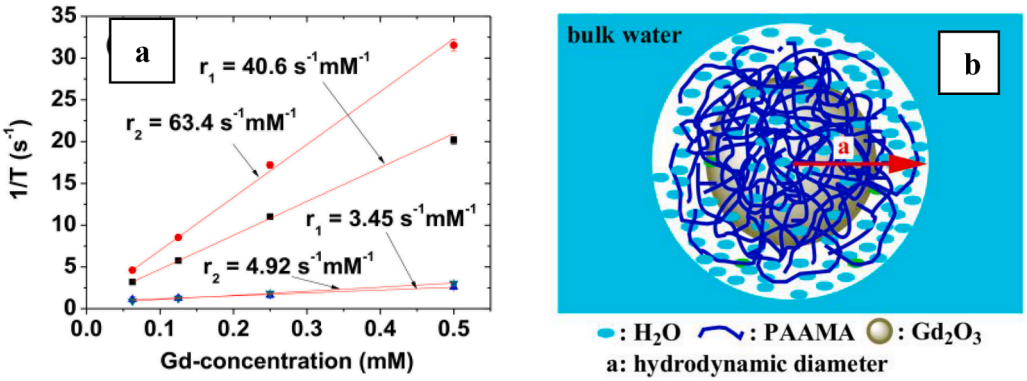

Fig. 22. (a)The r_1 and r_2 values of PAAMA-coated Gd_2O_3 nanoparticles (b) model showing many water molecules attracted by PAAMA-coated Gd_2O_3 nanoparticles, which utilises the hydrodynamics of large diameter (a) (Reprinted with permission from [47] Copyright © 2020 by Jang et al., MDPI).

groups per nanoparticle, PAAMA-coated ultrasmall Gd_2O_3 nanoparticles can strongly attract many water molecules to the nanoparticle surface, facilitating the diffusion of water molecules around the nanoparticles, thus leading to heavy hydration (large hydrodynamic diameter) (Fig. 22b). Therefore, many water molecules interact with many Gd^{3+} on the nanoparticle surface, achieving a very high r1 value based on the inner-sphere model [47,73]. Table 2 summarizes the relaxivity (r_1) values of Gd_2O_3 nanoparticles coated with various hydrophilic and biocompatible polymers. These polymers, which contain abundant carboxylic groups, present promising options as surface-coating ligands, enhancing the functionality of ultra-small Gd_2O_3 nanoparticles as T_1-weighted MRI contrast agents.

5.2. T_2 contrast agents

Nanoparticles based on lanthanide elements (Ln), such as Dy^{3+} ($^6H_{15/2}$), Ho^{2+} ($^5I_8$), and Tb^{3+} ($^7F_6$), exhibit magnetic moment components derived from the rapid orbital motion of 4f-electrons, inducing negligible longitudinal relaxation of water proton spins due to the swift electron movement separate from the slow proton spin motion [74,75]. Hence, Tb, Ho, and Dy-based materials are the best choice and suitable for ultra-high field T_2 MRI [7,12,15,17,31,32,46,54,58,61]. For example, Ln_2O_3 nanoparticles (Ln = Tb and Ho) show significant r_2 values in the 3.0 T MR field, which are 3.19 $mM^{-1}\,s^{-1}$ for Tb_2O_3 and 1.44 $mM^{-1}\,s^1$ for Ho_2O_3 coated with PAA. Furthermore, there is an increase in r_2 values in the 9.4 T MR field, which are 16.40 $mM^{-1}\,s^1$ for Tb_2O_3 and 9.20 $mM^{-1}\,s^1$ for Ho_2O_3 coated with PAA [32]. The r_2 value of lanthanide oxide nanoparticles is very sensitive to particle diameter, where larger particles tend to have higher magnetic nanoparticle (MNP) values [22]. The MNP can be estimated by assuming a spherical shape for the nanoparticles. In particular, the MNP value for Tb_2O_3 nanoparticles exceeds that of H_2O_3 nanoparticles, explaining why there is a larger r_2 value for Tb_2O_3-coated PAA nanoparticles compared to Ho_2O_3-coated PAA [38]. For comparison, the r_2 value of PAA-coated Ln_2O_3 (Ln = Tb and Ho) nanoparticles was compared with the r_2 value of D-glucuronic acid-coated Ln_2O_3 nanoparticles with Ln_2O_3 nanoparticles coated with D-glucuronic acid demonstrating larger diameters and higher r_2 values [7]. PAA-coated nanoparticles excel in retaining more water molecules due to their elongated chains and a higher count of carboxylic groups (~25 COOH groups per PAA), thereby inducing significant swelling in PAA-coated nanoparticles, substantially increasing the hydrodynamic diameter. Conversely, despite its smaller size compared to PAA, D-glucuronic acid might facilitate enhanced water molecule interaction due to its reduced dimensions. This interaction potentially elevates the r_2 value relevant to their response to magnetic fields, particularly in the context of MRI applications (Fig 23) [38]. However, the larger rod-shaped Tb_2O_3 nanoparticles demonstrate a higher r_2 value [9]. Nanoparticles with larger sizes exhibit higher magnetization values, consequently presenting a stronger magnetic resonance (MR) contrast effect [76,77].

The size and shape of lanthanide nanoparticles significantly influence relaxivity (r_2) or the ability of these nanoparticles to enhance T_2-weighted MRI signals. Ni et al. [4] demonstrated that increasing the size of $NaHoF_4$ nanoparticles increases the r_2 value in an ultra-high magnetic field of 7.0 Tesla, with 29 nm particles achieving the highest r_2 value (222.64 $mM^{-1}\,s^{-1}$). This improvement results from the larger particle volume, which supports increased magnetic interactions, thus enhancing the relativity effect. Additionally, Marasini et al. [32] found that larger Tb_2O_3 nanoparticles exhibit higher r_2 values than Ho_2O_3 nanoparticles in the 9.4 T field, affirming that the relativity value correlates positively with nanoparticle size.

The shape also plays a crucial role. González et al. [31] reported that rhombus-shaped HoF_3 nanoparticles (HoF-rh) possess a higher r_2 value (608.39 $mM^{-1}\,s^{-1}$) compared to elliptical-shaped particles (HoF-el), which have an r_2 of 349.98 $mM^{-1}\,s^{-1}$. This shape-dependent variation in magnetic distribution enhances relativity. In general, ellipsoid-shaped nanoparticles possess larger surface areas compared to rhombus-shaped nanoparticles with similar volumes. This distinction arises from their differing geometric structures with the ellipsoid's curved surface generating more area than the rhombus, characterized by simpler edges. This demonstrates that the geometric attributes of particles, particularly surface dimensions and shape, significantly impact the relative surface area despite a constant particle volume [31]. Additionally, although DyF-rh nanoparticles are of the same size as HoF-rh nanoparticles, their r_2 value (380.37 $mM^{-1}\,s^{-1}$) was lower. This discrepancy is intriguing since the effective moment of Dy^{3+} is slightly larger than the magnetic moment of Ho^{3+}[31]. These findings indicate that the HoF_3 and DyF_3 nanoparticles have great potential as contrast agents in high-field MRI scans.

Similarly, Kattel et al. [56] observed that dysprosium hydroxide nanorods yield a higher r_2 value (181.57 $mM^{-1}\,s^{-1}$) than spherical dysprosium oxide nanoparticles in a field strength of 1.5 T, as the elongated structure facilitates greater magnetic interactions. The effect of size and shape becomes more complex at higher magnetic fields, such as 9.4 T. Gómez et al. [58] found that the r_2 value of cubical $HoPO_4$ nanoparticles initially increases with size at both low and high fields but decreases at the largest size (80 nm) due to aggregation tendencies, indicating that colloidal stability is critical for maintaining relativity at high fields. Overall, both nanoparticle size and shape impact relativity, with larger sizes and specific geometries (e.g., nanorods or rhombic shapes) leading to increased relativity. These insights are essential for advancing MRI contrast agent design, enabling tailored nanoparticle size and shape for enhanced imaging across various magnetic fields.

These results are summarized in Table 3 which consolidates key findings on the influence of nanoparticle size, shape, and coating on relaxivity (r_2) values. Lanthanide-based nanoparticles, such as those derived from Dy^{3+}, Ho^{3+}, and Tb^{3+}, show distinct magnetic

Table 2
The r_1 values of various polymer-coated Gd_2O_3 nanoparticles.

Polymer	d_{avg} (nm)	a_{avg} (nm)	Temperature (°C)	Applied Field (T)	r_1 ($mM^{-1}\,s^{-1}$)	Ref
PAA	2.0	6.3	22	1.5	31.0	[8]
PASA	2.0	12.7	22	3.0	19.1	[72]
PAAMA	1.8	9.0	22	3.0	40.6	[47]
PMVEMA	1.9	19.8	22	3.0	36.2	[1]

PAA = polyacrylic acid; PASA = polyaspartic acid; PAAMA= polyacrylic acid-co-maleic acid; PMVEMA = polymethyl vinyl ether-alt-maleic acid.

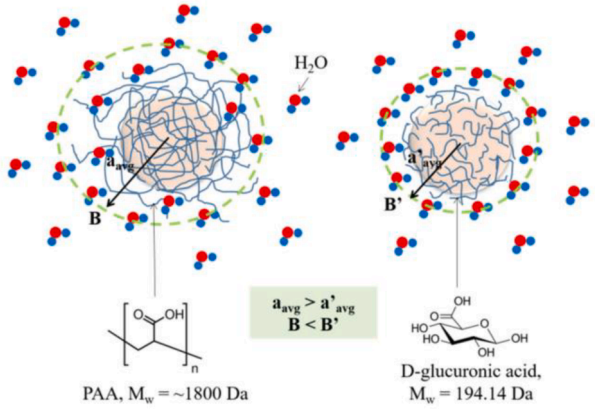

Fig. 23. Scheme explaining the ligand-size effects on hydrodynamic diameter and r_2 value. A_{avg} and $a_{avg'}$ = average hydrodynamic diameter; B and B' = magnetic field generated by the NPs (Reprinted with permission from [38] Copyright © 2021 by Marasini et al., MDPI).

properties influenced by their electronic structures and geometric characteristics. Specifically, the size and shape of lanthanide nanoparticles significantly affect their relaxivity values, with larger and more elongated nanoparticles typically demonstrating higher r_2 values due to increased magnetic interactions. Additionally, surface coatings such as PAA further enhance the relaxivity by increasing the hydrodynamic diameter and facilitating greater water molecule interactions with the nanoparticles. These insights are crucial for developing effective MRI contrast agents, as they highlight how nanoparticle design, both in terms of geometry and surface functionalization, can be tailored for optimal performance, particularly in ultra-high magnetic fields.

6. In vivo imaging and in vitro lanthanide nanoparticle

Nanoparticles have become a promising tool for cancer diagnosis and treatment by selectively accumulating in cancer tissues through enhanced EPR effects. The nanoparticles accumulate in tumours because of their extended circulation and larger hydrodynamic size, surpassing the threshold for renal clearance. This enables them to exit through leaky blood vessels specifically found in tumour areas, leading to their accumulation within the tumour tissue [78–80]. Nanoparticles accumulate in tumour tissues through passive targeting, active targeting, and circulation time in the body [42,81]. MRI contrast enhancement enables better visualization and delineation of tumours during planning, treatment and response assessment [82]. Several methods of synthesis and application of lanthanide-based nanoparticles as MRI contrast agents have been achieved through passive targeting and active targeting as discussed below.

6.1. T_1 contrast agent

Cai et al. [52] transformed gadolinium nanoplates using positively charged PEI, which facilitated cellular internalization. They further modified these functionalized nanoplates with hydrophilic PEG chains to create PEI-PEG complexes for use as MRI contrast agents. The encapsulated Gd_2O_3 formed biocompatible clusters coating the Gd_2O_3 nanoplates enabled T_1-weighted MRI. These clusters exhibited a remarkably high r_1 of 14.13 mM^{-1} s^{-1}, significantly surpassing the commercial contrast agent Gd-DTPA (r_1 = 3.40 mM^{-1} s^{-1}) (Fig. 24a and 24b). The biocompatibility of Gd_2O_3 nanoparticles was assessed using 293T, MCF-7, and SCC-7 cells, showing that the N-Dodecyl-PEI-PEG coating reduced the cluster toxicity derived from Gd_2O_3 nanoplates. As shown in Fig. 24c, cell viability above 80 % was observed in normal cells and cancer cells treated with the cluster solution even with a Gd (III) concentration of 66.0 μg/mL for 24 h. These findings suggest that the current cluster shows promise as a potential T1-weighted MRI contrast agent, offering significant contributions to the exploration of Gd_2O_3 nanoparticle-based MRI contrast agents in biomedical applications.

Wu et al. [42] synthesized nanoparticles by combining hyaluronic acid with Gd_2O_3 which exhibited a high longitudinal relaxivity

Table 3
The r_2 values of various size and shape of Ln_2O_3 nanoparticles.

Particle	Surface Modification	Size (nm)	Morphology	Applied Field (T)	r_2 (mM^{-1} s^{-1})	Ref
Tb_2O_3	D-Glucoronic acid	2.0	Spherical	9.4	58.33	[7]
Tb_2O_3	PEG	9.0	Nanorods	9.4	48.5	[9]
Tb_2O_3	PAA	1.8	Spherical	9.4	16.44	[38]
Ho_2O_3	PAA	1.7	Spherical	9.4	9.20	[38]
HoF_3	EG	110	Elipsoidal	9.4	608.39	[31]
DyF_3	EG	110	Rhombus	9.4	380.37	[31]

EG = ethylene glycol; PAA= polyacrylic acid; PEG = polyethylen glycol.

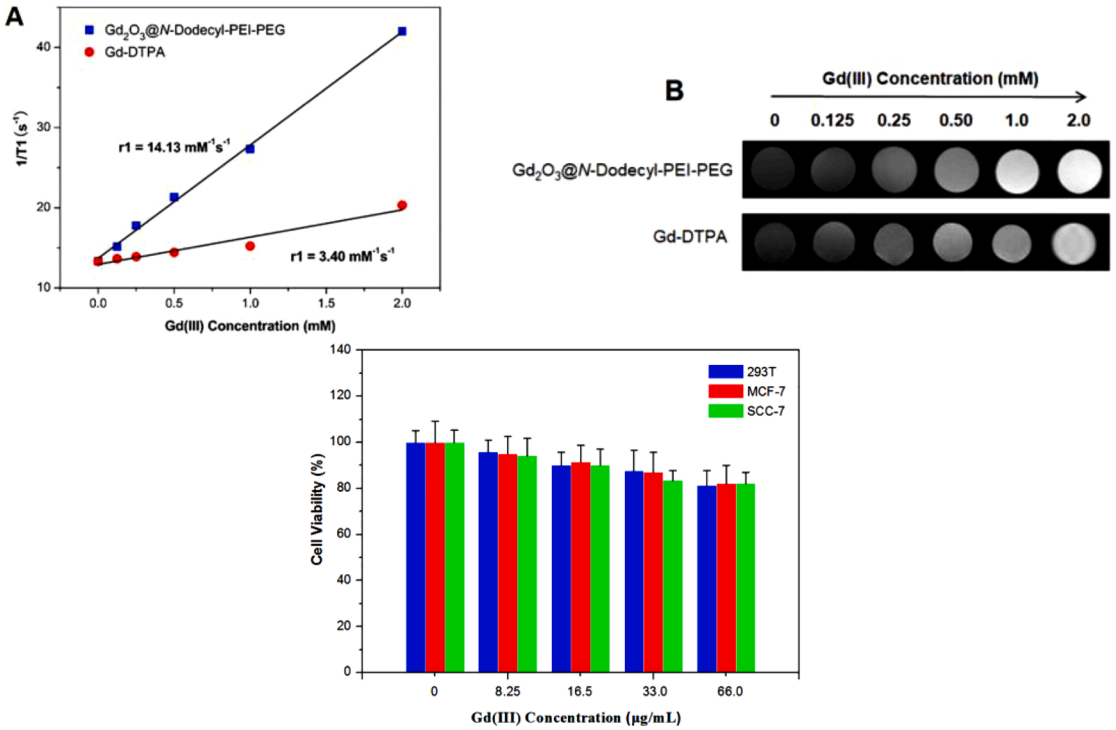

Fig. 24. (a) Longitudinal relaxivity (r_1) of the Gd_2O_3@N-Dodecyl-PEI-PEG cluster and commercial Gd-DTPA. (b) Solution MR images of the cluster and commercial Gd-DTPA (Gd(III) concentrations of 0, 0.125, 0.25, 0.50, 1.0, and 2.0 mM, respectively. (c) Cell viability of Gd_2O_3@N-Dodecyl-PEI-PEG (293T, MCF-7 or SCC-7 cells cultured with cluster solutions containing various concentrations of Gd(III) for 24 h (Reprinted with permission from [52] Copyright © 2019, Elsevier).

value (r_1) of 6.0 mM^{-1} s^{-1} as an MRI contrast agent, surpassing the commercial MRI contrast agent (Magnevist) with a r_1 of 3.86 mM^{-1} s^{-1}. The biocompatibility of the HA-Gd_2O_3 nanoparticles was assessed in HepG2 and VSMC cells, revealing no cytotoxic effects with cell viability ≥90 % even at HA-Gd_2O_3 concentrations up to 200 μg/L. The introduction of hyaluronic acid enhances water dispersibility, lowers cytotoxicity, and ensures excellent biocompatibility for Gd_2O_3. Furthermore, they exhibit radiosensitization enhancement in a dose-dependent manner, underscoring their potential in both tumour diagnosis and radiotherapy applications.

Ho et al. [83] synthesized PAA-Gd_2O_3 nanoparticles conjugated with the tumour-targeting ligands folic acid (FA) and/or cyclic arginylglycylaspartic acid (cRGD). FA targeting folate receptors overexpressed on tumour cells facilitating nanoparticle penetration may increase plasma concentrations around tumour cells to achieve more contrast [62,84–88]. Conversely, cRGD peptides target integrin receptors (e.g., αvβ3) overexpressed on tumour cells linked to processes such as angiogenesis and tumour metastasis [89]. The

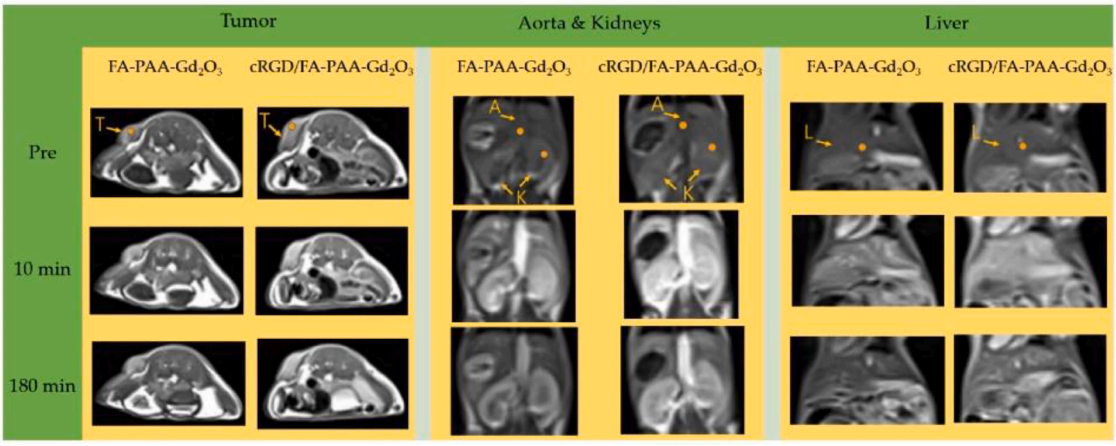

Fig. 25. T1 MR images at 3.0 T, labelled as "Pre," and after injecting aqueous suspensions of FA-PAA-Gd_2O_3 and cRGD/FA-PAA-Gd_2O_3 nanoparticles intravenously into mice tails (Reprinted with permission from [77] Copyright © 2022 the Ho et al., MDPI).

cRGD/FA-PAA-Gd_2O_3 nanoparticles exhibited a high longitudinal r_1 of 11.2 mM^{-1} s^{-1}, approximately four times higher than those of commercial MRI contrast agent (Gd-DTPA) with a value of 3.1 mM^{-} $1s^{-1}$ [90]. In vivo imaging (Fig. 25) showed that cRGD/FA PAA-Gd_2O_3 nanoparticles, which featured multiple tumour-targeting ligands, exhibited superior contrast in tumour sites compared to FA-PAA-Gd_2O_3 nanoparticles with a single tumour-targeting ligand. Additionally, cRGD/FA-PAA Gd_2O_3 nanoparticles exhibited enhanced contrast in all organs, especially in the aorta, attributed to the blood cell-shedding effect of cRGD increasing their circulation in the bloodstream. The biocompatibility of FA-PAA-Gd_2O_3 and cRGD/FA PAA-Gd_2O_3 nanoparticles was assessed in NCTC1469 normal and U87MG tumour cells with NCTC1469 cells showing good viability even when exposed to 500 μM Gd (Fig. 26). However, there was a decrease in viability of U87MG cells as the Gd concentration increased. When the Gd concentration reached high levels, an increase in cellular toxicity was observed in cRGD/FA-PAA-Gd2O3 nanoparticles compared to FA-PAA-Gd_2O_3 nanoparticles due to the dual targeting performed by cRGD and FA on cRGD/FA-PAA-Gd_2O_3 nanoparticles [83].

An in vitro study of core-shell salicylic acid-gadolinium (Gal-PEG-2000) using HepG-2 cells demonstrated that Gal-PEG-750, Gal-PEG-2000, and Gal-PEG-5000 composite nanoparticles exhibited minimal toxicity, with cell viability remaining above 85 % even at a Gd^{3+} concentration of 320 μg/L (Fig. 27a). This excellent biocompatibility is due to the protective PEG coating. Furthermore, in vivo imaging studies confirmed the effectiveness of Gal-PEG-2000 as a contrast agent (Fig. 27b). T_1-weighted MR images of mice revealed increased liver brightness 1 h after injection, indicating rapid distribution through the body. The enhanced signal persisted for up to 3 h, followed by increased intestinal brightness, suggesting metabolism and excretion via the liver. The liver brightness significantly decreased by 6 h confirming nanoparticle clearance. This prolonged retention time enables repeated imaging with lower contrast agent doses, reducing potential side effects while emphasizing the nanoparticles' biocompatibility and liver-specific metabolism for imaging applications [59].

6.2. T_2 contrast agent

The efficacy of the nanoparticles as MRI T_2 contrast agents in high MR fields was assessed through in vivo T_2 MR imaging at 9.4 T with additional imaging at 3.0 T for comparison. The images captured 15 min after administration showed increased negative contrast (darker appearance) in the liver and kidney compared to images before administration in both 3.0 T and 9.4 T MR fields. The stronger negative contrast in 9.4 T compared to 3.0 T was due to higher r_2 values at higher magnetic fields [32]. Dy_2O_3 nanoparticles can also be used as a contrast agent for T_2-based MRI as they exhibit relativity values of 2.0 mM^{-1} s^{-1} at 3.0 T and 11.31 mM^{-1} s^{-1} at 9.4 T. Fig. 28 presents the in vivo T_2 MRI testing at 3.0 T which shows a clear negative contrast enhancement in the liver. In addition, the SNR plot shows the contrast change in the liver up to 3 h after intravenous injection, indicating that PAA-coated Dy_2O_3 nanoparticles are an effective T_2 contrast agent in MRI [12].

The in vitro and in vivo evaluations demonstrated the biocompatibility and efficacy of DYO@C nanoparticles as T_2 MRI contrast agents. As shown in Fig. 29a, the cell viability of DU145 human prostate cancer cells and NCTC1469 normal mouse hepatocyte cells remained above 80 % at Dy concentrations up to 500 μM, indicating good biocompatibility. In contrast, uncoated DYO nanoparticles exhibited significant cytotoxicity at concentrations exceeding 50 μM, underscoring the importance of the carbon coating for biomedical applications. In vivo MRI studies in mice revealed clear negative contrast enhancements in the kidneys following intravenous administration of DYO@C nanoparticles (Fig. 29b). These darkened contrasts reached a maximum at 30 min post-injection and gradually diminished, returning to baseline levels, consistent with renal excretion. No noticeable contrast changes were observed in the liver, likely due to rapid nanoparticle clearance within 30 min (Fig. 29c). The nanoparticles' high r_2/r_1 relativity ratio contributed to their effectiveness as T_2 MRI contrast agents, demonstrating behaviour comparable to commercial molecular agents and validating their potential for biomedical imaging.

The cytotoxicity of PEG-TbNRs (0.1 to 100 μg/mL) was evaluated in vitro using cell morphology, live-dead, and MTT assays in the mouse microglial cell line N13 (Fig. 30a-c). There were no morphological changes, no significant increase in cell death, and no impact on mitochondrial activity, indicating excellent cellular biocompatibility. Additionally, in vivo T_2 MR images in 9.4 T showed significant negative contrast enhancements in the liver and kidneys following intravenous injection, further confirming their suitability as MRI contrast agents [9].

Furthermore, Gonzalez et al. [91] measured the transverse proton relaxation times (T_2) of $Ba_{51}Dy_{49}$ nanoparticles in aqueous

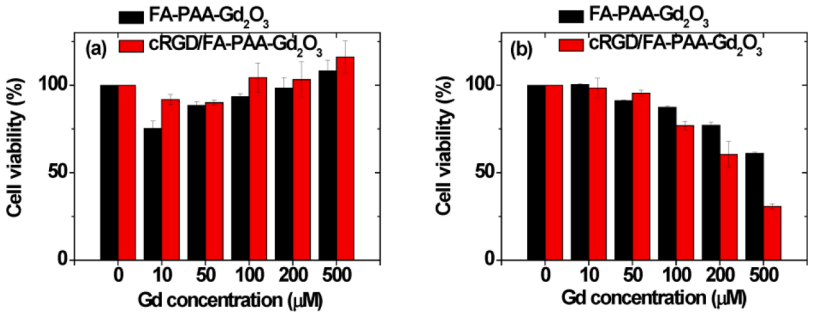

Fig. 26. The effect of nanoparticles on the viability of (a) NCTC1469 (normal) and (b) U87MG (tumour) cells after 48 h of incubation with FA-PAA-Gd_2O_3 and cRGD/FA-PAA-Gd_2O_3 nanoparticles (Reprinted with permission from [77] Copyright © 2022 by Ho et al., MDPI).

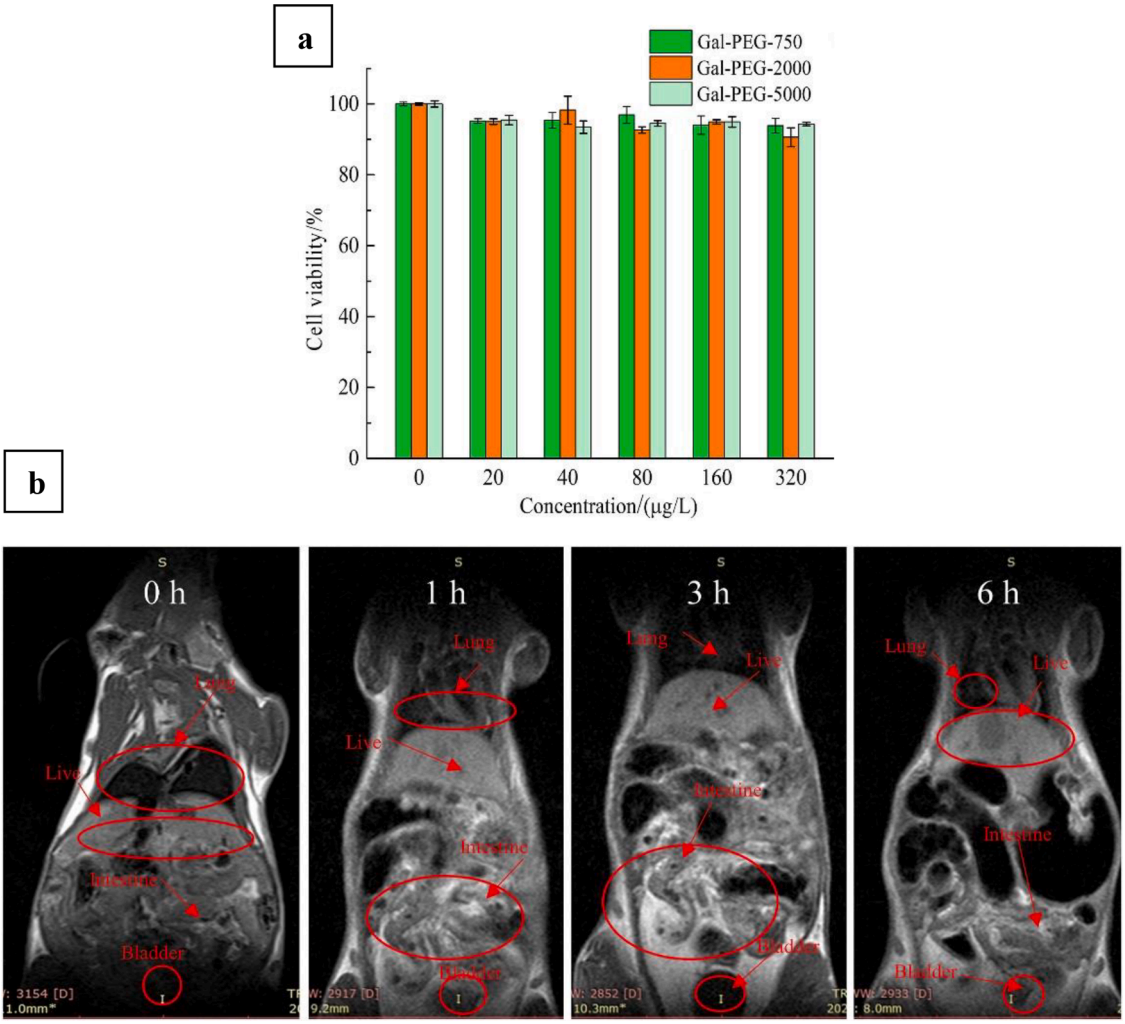

Fig. 27. The viability of HepG-2 cells following exposure to various concentrations of Gal-PEG-750, Gal-PEG-2000, and Gal-PEG-5000; (b) presents in vivo MR imaging of Gal-PEG-2000 captured at 1, 3, and 6 h post-injection via the tail vein (Reprinted with permission from [59] Copyright © 2021, Elsevier).

suspensions at various concentrations in both conventional (1.44 T) and ultra-high (9.4 T) magnetic fields. The plots of $1/T_2$ against Dy^{3+} concentration demonstrated a linear relationship, indicating the absence of particle aggregation, which is consistent with stability data (Fig. 31). The r_2 were 11.34 $mM^{-1}{\cdot}s^{-1}$ at 1.44 T and 147.11 $mM^{-1}{\cdot}s^{-1}$ at 9.4 T, with the r_2 value at the ultra-high field significantly surpassing that of other Dy^{3+}-based nanoparticles (91.4 and 101 $mM^{-1}{\cdot}s^{-1}$). This higher r_2 value indicates enhanced MRI contrast, particularly in elevated magnetic fields. Additionally, Ba51Dy49 nanoparticles exhibited very low toxicity in HFF-1 fibroblasts. Cell morphology remained unchanged and mitochondrial activity did not decrease below 75 %, even at the highest nanoparticle concentration tested (380 μg $Dy{\cdot}mL^{-1}$). These findings suggest that the nanoparticles do not induce necrosis or apoptosis, rendering them highly suitable candidates for nanomedicine applications.

Comprehensive in vitro and in vivo studies are critical to assess the effectiveness and safety of nanoparticles for biomedical applications. In vitro studies using cell models provide valuable preliminary data on biocompatibility, cytotoxicity, and internalization efficiency, whereas in vivo studies using animal models are essential for evaluating nanoparticle biodistribution, accumulation, and overall biological effects in living systems. Furthermore, the success of nanoparticle-based applications hinges on the strategy employed, whether through active targeting, which leverages specific molecular interactions or passive targeting utilizing the EPR effect. Lanthanide nanoparticles demonstrate significant potential in biomedical applications, particularly as MRI contrast agents and in cancer therapy, underscoring the importance of rigorous safety evaluations. Table 4 summarizes in vitro and in vivo studies on developing lanthanide nanoparticles as T_1 and T_2 contrast agents. Lanthanide-based nanoparticles exhibit acceptable cytotoxicity at concentrations relevant to medical applications. Moreover, the in vivo findings highlight their favourable accumulation in target tissues, prolonged retention times, and safe systemic distribution at therapeutic doses. Functionalization strategies can enhance their biocompatibility, targeting specificity, and therapeutic efficacy. Nevertheless, comprehensive investigations are still required to

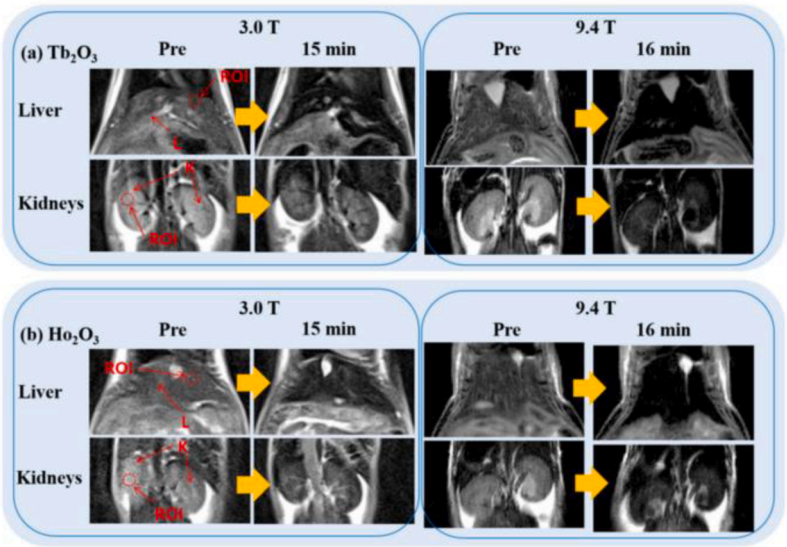

Fig. 28. In vivo T_2 MR images of the liver and kidneys were taken at both 3.0 and 9.4 T MR fields before (labelled as "Pre") and 15 (or 16) minutes post-intravenous administration of aqueous suspension samples containing PAA-coated (a) Tb_2O_3 and (b) Ho_2O_3 nanoparticles into mice tails (Reprinted with permission from [38] Copyright © 2021 by Marasini et al., MDPI).

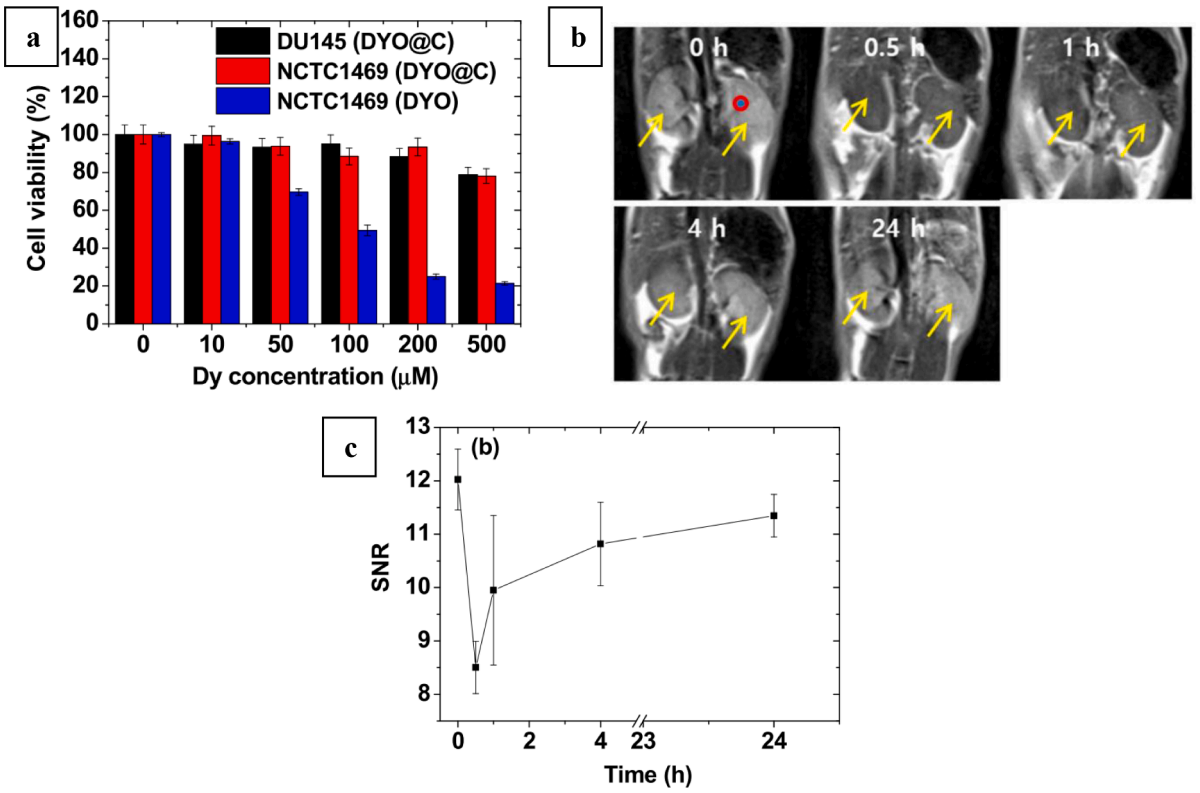

Fig. 29. (a) Cell viabilities of DYO@C nanoparticles in NCTC1469 and DU145 cells, compared to DYO nanoparticles (before carbon coating) in NCTC1469 cells. (b) Coronal T2 MR images of mice kidneys (indicated by arrows) at various time points, with a region-of-interest (ROI) highlighted by a small circle used for signal-to-noise ratio (SNR) analysis. (c) SNR plot of the ROI as a function of time, showing preadministration at 0 h and subsequent time points after intravenous administration of the aqueous DYO@C nanoparticle solution into the tail veins of four mice (Reprinted with permission from [15] Copyright © 2020 by Yue et al., MDPI).

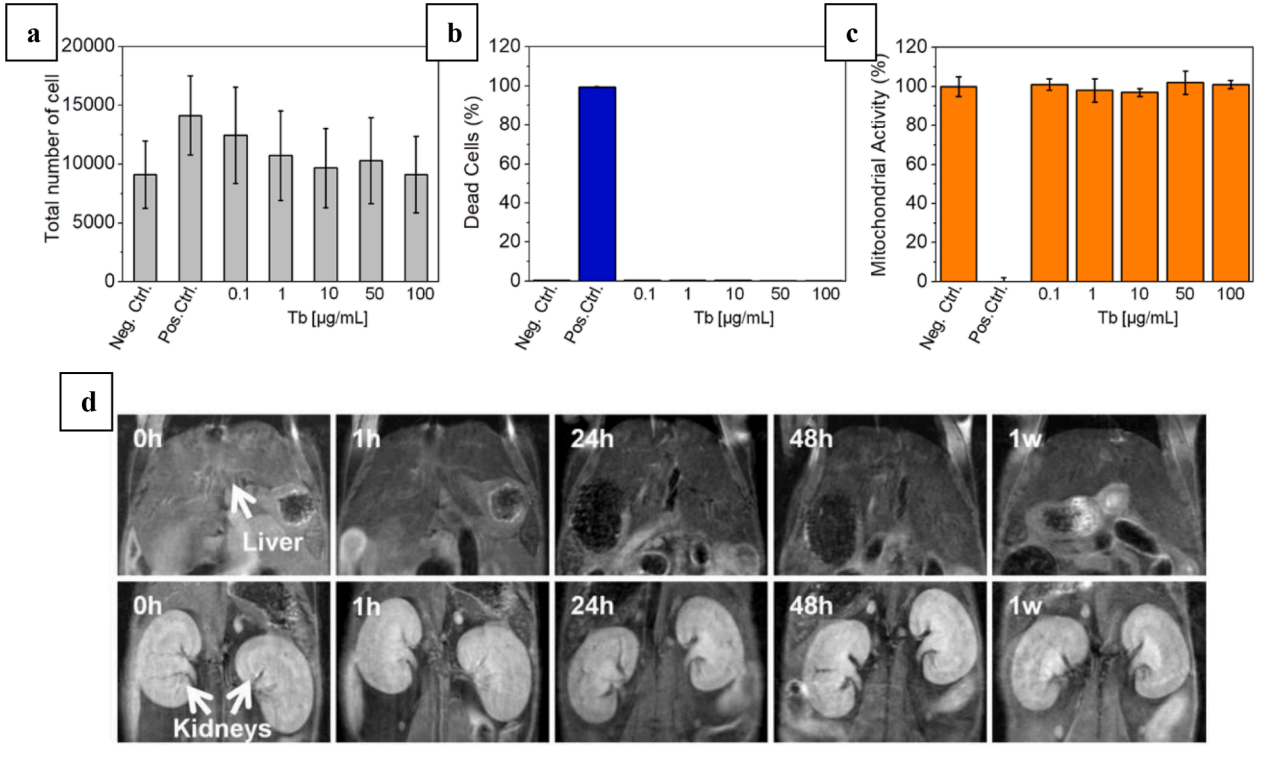

Fig. 30. The in vivo pharmacokinetics of PEG-TbNRs administered intravenously to BALB/c mice are illustrated with T2-weighted MR images taken at various time points post-injection. The scale bars represent 100 µm. The bar graphs show: (a) the total cell count per well, (b) the percentage of dead cells, and (c) cell viability following exposure to increasing concentrations of PEG-TbNRs for 24 h. (Reprinted with permission from [9] Copyright © 2021 *American Chemical Society*).

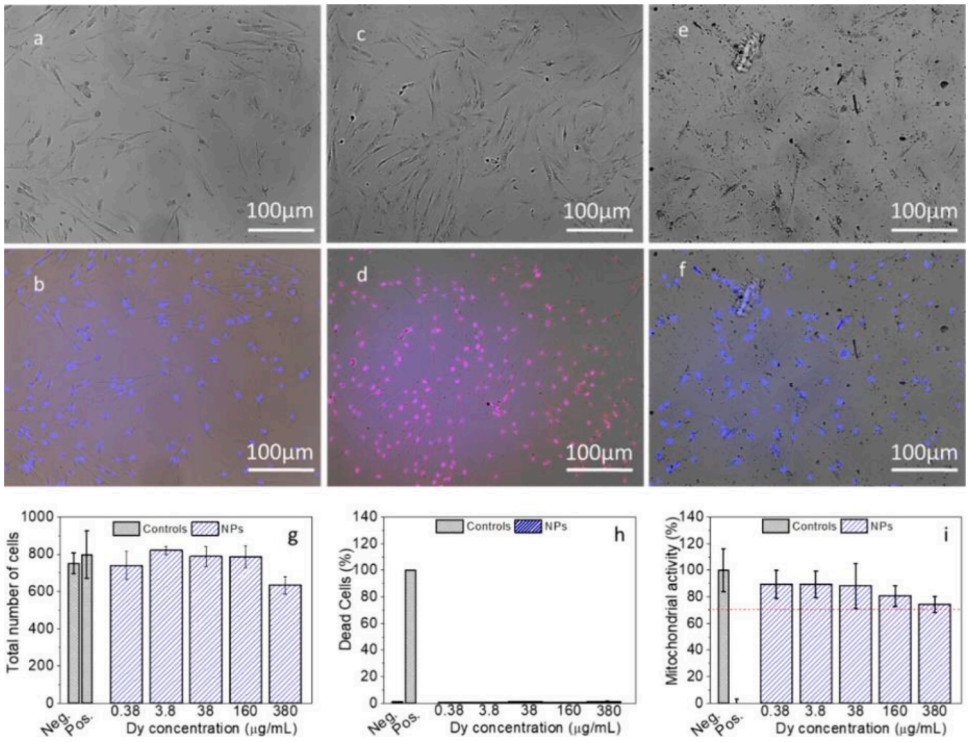

Fig. 31. Bright-field optical microscopy images show HFF-1 fibroblast cells (top), while the lower images present merged views combining bright-field microscopy with fluorescence images stained by Hoechst 33,342 (blue) and TO-PRO-3 iodine (red). Panels (a, b) depict the negative control, (c, d) show the positive control, and (e, f) illustrate cells exposed to 380 $\mu g \cdot mL^{-1}$ of Ba51Dy49 nanoparticles. Graph (g) displays the total number of cells per well following exposure to increasing concentrations of nanoparticles, (h) shows the percentage of dead cells, and (i) presents the results of the MTT assay, indicating cell viability after nanoparticle exposure (Reprinted with permission from [84] Copyright © 2024 American Chemical Society).

elucidate their long-term effects and potential chronic toxicity, particularly for clinical translation.

7. Multifunctional potential of nanoparticles: combining imaging and therapy for theranostic applications

Nanoparticles have emerged as versatile tools in biomedical applications due to their unique physicochemical properties, including tunable size, surface modification capabilities, and high biocompatibility [92–95]. Initially, their primary role was to enhance imaging modalities such as MRI enabling more precise diagnostics. However, recent advancements have revealed their potential for therapeutic applications, paving the way for developing theragnostic-integrated systems that combine diagnostics and therapy within a single platform. The dual functionality of nanoparticles offers significant advantages in cancer management, particularly by enabling early detection and targeted treatment while minimizing off-target effects. For instance, functionalized nanoparticles can be designed to act as MRI contrast agents and simultaneously deliver therapeutic payloads, such as chemotherapeutic drugs, and genes, or through techniques like magnetic hyperthermia. Furthermore, their potential for multimodal imaging combining MRI with other imaging modalities such as PDT, PTT, CT, or fluorescence underscores their utility in achieving comprehensive tumour visualization and monitoring treatment responses.

Recently, the combination of photodynamic therapy (PDT) and photothermal therapy (PTT) has generated considerable interest as an alternative to chemotherapy and radiotherapy in cancer treatment [96]. PDT uses photosensitizers that interact with oxygen to produce ROS when exposed to light, while PTT utilizes hyperthermia generated by photothermal agents. Both therapies offer significant advantages, including minimal invasiveness, low toxicity, reduced long-term mortality, and high therapeutic selectivity and effectiveness [97,98]. Chen et al. [99] demonstrated the potential of gadolinium-porphyrin-based polymer nanotheranostics (Gd–PNPs) as effective imaging-guided PDT agents for cancer treatment. Gd-PNPs demonstrated 1.6 times stronger fluorescence and superior MR imaging capabilities compared to Gd-TCPP, showing a 3.5-fold increase in MR signal at the tumour site due to the EPR effect. In PDT, the production of singlet oxygen ($^1O_2$) by Gd-PNPs increased with concentration and longer laser exposure, achieving similar efficiency to TCPP and Gd-TCPP. In vivo, combining Gd-PNPs with laser irradiation resulted in significant tumour inhibition in CT 26 tumour-bearing mice, reducing both tumour volume and weight with no observed systemic side effects. These results suggest that Gd-PNPs have great potential for use in imaging-guided PDT for cancer therapy.

Similarly, Zhang et al. [2] highlighted the potential of HoF_3 nanoparticles as dual-modal imaging (CT and MRI) agents for cancer diagnosis. The rapid advancements in medical imaging have led to the growing importance of dual-modal imaging for cancer

Table 4
Summary of synthesis, characterization, and application of lanthanide nanoparticles as MRI contrast agent.

Particle	Preparation Method	Surface Modification	Size (nm)	Morphology	ζ (mV)	r_1 (mM^{-1} s^{-1})	In Vitro and In Vivo Studies	Reference
Gd_2O_3	Thermal Decomposition	PEI-PEG	95	Spherical	+23.73	14.13	N-dodecyl-PEI-PEG-coated Gd_2O_3 clusters showed >80 % viability in 293T, MCF-7, and SCC-7 cells at 66.0 μg/mL Gd (III) after 24 h	[52]
Gd_2O_3	One-pot hydrothermal	HA	105	Spherical	–	6.0	Cell viability remained ~90 % in HepG2 and VSMC cells even at 200 μg/mL after 24 h and up to 3 days of incubation, indicating excellent biocompatibility	[42]
Gd_2O_3	One-pot polyol	poly(methyl vinyl ether-alt-maleic acid) (PMVEMA)	1.9	Spherical	–	36.2	Demonstrates good biocompatibility with DU145 cells at Gd concentrations up to 500 μM; PMVEMA-coated NPs also show excellent colloidal stability, with no precipitation and a clear Tyndall effect, confirming stable dispersion	[1]
Gd_2O_3	One-pot polyol	poly(acrylic acid-co-maleic acid) (PAAMA)	1,8 ± 0,1	Spherical	−43,9 ± 0,2	40.6	PAAMA-coated ultrasmall Gd_2O_3 nanoparticles showed no toxicity up to 500 μM Gd in DU145 and NCTC1469 cells. T1 MRI images showed liver and kidney contrast enhancement, with SNR peaking at ~30 min post-administration and decreasing due to excretion.	[47]
Gd_2O_3	Polyol	FA-PAA[1] cRGD/FA-PAA[2]	1,7[1] 1,7[2]	Spherical	−33,9[1] −16,6[2]	12[1] 11,2[2]	NCTC1469 cells showed good viability at up to 500 μM Gd, with toxicity increasing at higher concentrations; NP 2 was more toxic than NP 1 due to enhanced targeting, while NP 1 exhibited higher contrast, particularly in the aorta, due to longer circulation time	[83]
Gd_2O_3	Polyol	DEG[1] TEG[2] TeEG[3] PEG[4]	13±2[1] 16 ±22[2] 19±2[3] 21±2[4]	Spherical	–	1,14 [1] 2,60 [2] 3,99 [3] 5,75 [4]	PEG-Gd_2O_3 demonstrates excellent biocompatibility with HEK 293 cells, showing no significant decrease in cell viability up to a concentration of 1 mM after 24 h of incubation	[55]
$HoPO_4$	Polyol	PAA	24 [1] 48 [2] 80 [3]	Cube	–	382,91 [1] 489,91 [2] 166,38 [3]	Cellular toxicity of Ho^2 was assessed in HFF-1 human foreskin fibroblasts, showing no significant toxic effects even at the high concentration of 100 μg/mL and demonstrated excellent colloidal stability in a physiological medium (PBS)	[58]

(*continued on next page*)

Table 4 (*continued*)

Particle	Preparation Method	Surface Modification	Size (nm)	Morphology	ζ (mV)	r_1 (mM^{-1} s^{-1})	In Vitro and In Vivo Studies	Reference
Ho_2O_3	Polyol	PAA	1,7 ± 0.1	Spherical	−32.9 ± 0.1	3.0 T 1.44 and 9.4 T 9.20	Exhibits good biocompatibility with DU145 and NCTC1469 cells maintaining >90 % at Ho concentrations up to 500 μM	[32]
$HoVO_4$	Polyol	PAA	60	Spherical	–	424	Cellular toxicity was assessed in the PC3 cell line, maintaining >70 % at $HoVO_4$ nanoparticle concentrations up to 150 μg/mL	[61]
Ho_2O_3	Polyol	D-glucuronic acid	1.9	Spherical	0,0578	7.76 mM^{-1} s^{-1} at 1.5 T, 35.21 mM^{-1} s^{-1} at 3 T, and 56.33 mM^{-1} s^{-1} at 9.4 T	Exhibits good biocompatibility with DU145 cells, maintaining >80 % at Ho concentrations up to 200 μM	[7]
Ho_2O_3	Polyol	PEI_{1200} [1] PEI_{60000} [2]	2.05 [1] 1.90 [2]	Spherical	19,9 [1] 20,7 [2]	13.1 [1] 9.9 [2]	Cellular toxicity Ho_2O_3 was assessed in DU145 cells 48 h after incubation, maintaining >80 % at Ho concentrations up to 500 μM	[33]
HoF_3	Solvothermal	PEG	30–55	Spherical	5.83	117.51	Cytotoxicity of PEG-HoF_3 NPs was evaluated via MTT assay on HeLa and L929 cells, showing ~85 % viability at 300 mg/mL. T_2-weighted MRI at 1, 2, 4, 12, and 24 h post-injection revealed no significant tumour signal change within 2 h; the signal decreased markedly by 12 h forming a dark area, and the tumour centre was filled with the contrast agent at 24 h	[46]
Tb_2O_3	Polyol	PAA	1,8 ± 0.1	Spherical	−25 ± 0.1	3.0 T MR field, which is 3.19 mM^{-1} s^{-1}. And at 9.4 T MR field, 16.40 mM^{-1} s^{-1}	Exhibits good biocompatibility with DU145 and NCTC1469 cells maintaining >90 % at Tb concentrations up to 500 μM.	[32]
Tb_2O_3	Polyol	D-glucuronic acid	2	Spherical	−0,0216	7.68 mM^{-1} s^{-1} at 1.5 T, 33.97 mM^{-1} s^{-1} at 3 T, and 53.67 mM^{-1} s^{-1} at 9.4 T	Exhibits good biocompatibility with DU145 cells, maintaining >80 % at Tb concentrations up to 200 μM	[7]
Tb_2O_3	Thermal Decomposition	PEG	9.0 × 2.1	Nanorods	–	in magnetic fields of 1.44 10.4 mM^{-1} s^{-1} and 9.4 T, showing 48.5 mM^{-1} s^{-1}	Cellular toxicity was evaluated in the mouse microglial cell line, N13, which demonstrated excellent biocompatibility, maintaining cell viability >80 % across Tb concentrations ranging from 0.1 to 100 μg/mL.	[9]
$DyVO_4$	Polyol	PAA	~60	Spherical	–	460 mM^{-1} s^{-1}	Cellular toxicity $NdVO_4$ was assessed in PC3 cell line, maintaining >70 % at $NdVO_4$ nanoparticle	[61]

(*continued on next page*)

Table 4 (*continued*)

Particle	Preparation Method	Surface Modification	Size (nm)	Morphology	ζ (mV)	r_1 (mM^{-1} s^{-1})	In Vitro and In Vivo Studies	Reference
							concentrations up to 300 μg/mL	
Dy_2O_3	Polyol	D-glucuronic acid	2,1	Spherical	0,0314	at 1.5 T, 37.52 mM^{-1} s^{-1} at 3 T, and 58.33 mM^{-1} s^{-1} at 9.4 T	Exhibits good biocompatibility with DU145 cells, maintaining >80 % at Dy concentrations up to 200 μM	[7]
Dy_2O_3	Polyol	Carbon (C)	3.0 ± 0.1	Spherical	−40.0 ± 0.2	5.7	Exihibits good biocompatibility with DU145 and NCTC1469, maintaining >80 % viability at Dy concentrations up to 500 μM and showed negative kidney contrast enhancement peaking at 30 min post-injection, consistent with renal excretion, with no significant liver contrast changes.	[15]
$NaDy(MoO_4)_2$	Polyol	PAA	23 [1] 50 × 16 [2] 68 × 20 [2] 87 × 22 [2]	Spheres [1] Ellipsoids [2]	−30 [1] −28[2]	160 to 220 mM^{-1} s^{-1} as their size grew from 50 × 16 to 87 × 22 nm. for 230 mM^{-1} s^{-1}	The cytotoxicity of NaDy $(MoO_4)_2$ NPs was evaluated in HFF-1 fibroblasts using the MTT assay, showing ~100 % cell viability at concentrations up to 100 μg/mL (0.61 mM Dy).	[54]

diagnostics, and HoF_3 nanoparticles (HoF_3 NPs) show great potential as a combined X-ray computed tomography (CT) and T_2-weight MRI probe due to Ho's high atomic number, intrinsic paramagnetic, and strong X-ray attenuation. A study developed PEGylated HoF3 NPs, demonstrating excellent biocompatibility with over 85 % cell viability in both HeLa and L929 cells, even at concentrations as high as 300 mg/mL. In vivo, PEG-HoF3 NPs showed superior contrast in CT imaging compared to iodine-based contrast agents, requiring lower doses for similar effects, which could minimize risks associated with large doses of contrast agents. Tumour-bearing mice exhibited significant contrast at the tumour site 24 h post-injection, with enhanced liver uptake, while no enhancement was observed in the kidneys, suggesting reduced kidney-related side effects. These findings highlight the promising potential of PEG-HoF_3 NPs for dual-modal imaging with excellent biocompatibility and imaging efficacy.

Jiang et al. [100] developed Gd-doped iron oxide nanoparticles (GdIONP), combining therapeutic and diagnostic functions, particularly for tumour therapy and MRI tracking. In their study, GdIONP accumulated in transgenic prostate adenocarcinoma tumours in C1 mice (TRAMP-C1). The results most indicative of GdIONP's potential for cancer therapy, combining radiotherapy (RT) and hyperthermia (TT), are the prolonged tumour growth delays observed in the RT + TT combination group which were significantly longer than the 2.5-day delay in the TT-only group and the 4.5-day delay in the RT-only group. Furthermore, immunohistochemical analysis revealed reduced hypoxic areas, vascular disruption, and extensive tumour necrosis in the combined treatment group, suggesting more effective tumour destruction. These results demonstrate that GdIONP can enhance cancer therapy by leveraging the dual effects of hyperthermia and radiotherapy.

Zhang et al. [101] synthesized Ho(III)-doped mesoporous polydopamine (Ho-MPDA) nanospheres loaded with mitoxantrone (MTO) and coated with 4T1 cell membranes (HMM@T), developing them as a theragnostic nanodrug for MRI-guided chemo-photothermal therapy of breast cancer. These nanoparticles displayed excellent T_2 MRI contrast properties ($r_2 = 152.13\ mM^{-1}s^{-1}$), high drug loading efficiency (18.4 %), and enhanced intracellular uptake facilitated by 4T1 cell membrane wrapping. Confocal microscopy revealed that HMM@T were internalized into lysosomes within 4 h, where the acidic pH and high GSH levels triggered efficient drug release. The cytotoxicity assays demonstrated significantly higher toxicity of HMM@T NPs toward 4T1 cells compared to Hepa1–6 cells or free MTO, confirming their selective breast cancer-targeting ability. In vivo, fluorescence imaging revealed rapid tumour accumulation and prolonged retention of HMM@T NPs, with peak signals observed at 8 h and sustained for up to 48 h. MRI and photoacoustic imaging (PAI) showed strong signal intensity at tumour sites, proving their efficacy as dual-mode imaging agents. Additionally, reduced nanoparticle accumulation in the liver and spleen indicated decreased clearance by the reticuloendothelial system, which enhanced tumour targeting.

Hye et al. [102] developed porous silicon nanoparticles coated with gadolinium silicate (pSiNPs-Gd) as an MRI contrast agent and drug delivery carrier by encapsulating anticancer drugs (SN-38, doxorubicin). pSiNPs-Gd exhibited excellent biocompatibility and high drug-loading efficiency, with 33.72 % for SN-38 and 24.54 % for doxorubicin (DOX). The drug release profile showed that half of the drug was released within 4 h, with the remaining drug released within 24 h, where the release of DOX was faster than that of SN-38.

Overall, this study demonstrates that pSiNPs-Gd can be used as an efficient and safe drug delivery carrier in biological systems and has the potential to serve as an effective nanomedicine platform for MRI contrast-based therapy and drug delivery. Furthermore, Shirazi et al. [103] reported the development of a cyclic peptide containing five tryptophan, five arginine, and one cysteine amino acids [(WR)5C], which was used to produce peptide-capped gadolinium nanoparticles [(WR)5C]-GdNPs, demonstrating their potential as an efficient siRNA delivery system. At a concentration of 50 μM, the nanoparticles exhibited minimal cytotoxicity (~93 % cell viability) in human leukaemia T lymphoblast cells (CCRF-CEM) and triple-negative breast cancer cells (MDA-MB-231) after 48 h. FACS analysis revealed more than a 10-fold increase in the cellular uptake of Alexa-488-labeled siRNA compared to siRNA alone. The nanoparticles effectively reduced STAT-3 protein expression (~62 %) in MDA-MB-231 cells, indicating successful gene silencing. Confocal microscopy confirmed enhanced siRNA internalization in MDA-MB-231 cells, and TEM analysis showed nanoparticles within the 240–260 nm size range. Flow cytometry further demonstrated the efficiency of [(WR)5C]-GdNPs as a siRNA transporter, suggesting their potential as a nontoxic transfection agent for nucleic acid-based therapeutics. The findings indicate that [(WR)5C]-GdNPs could be extended for use in other nucleic acid delivery applications, including microRNA or CRISPR/Cas9-based therapies.

The integration of imaging and therapy in nanoparticles has unlocked new possibilities for theragnostic applications in cancer treatment. By combining diagnostic and therapeutic functions within a single nanoparticle platform, these multifunctional nanomaterials enable more effective and personalized treatment strategies, offering significant benefits such as early detection, precise targeting, and reduced side effects. The studies discussed here illustrate the promising potential of various nanoparticle-based systems for improving cancer diagnosis and therapy. With further advancements in nanotechnology, these theragnostic platforms have the potential to revolutionize cancer care, enhancing both the efficacy and safety of cancer treatments.

8. Conclusion

MRI is the most powerful imaging technique because it is non-invasive and achieves good soft tissue contrast. MRI contrast agents are required to increase the sensitivity of MRI images and the use of nanoparticles has shown several advantages including a small particle size (<100 nm) and high surface ratio. Also, more lanthanide ions will increase their paramagnetic properties and improve MRI image results. Nanoparticles can also reduce the required dose thereby reducing toxicity. Nanoparticles based on lanthanides (Ho^{3+}, Dy^{3+}, Tb^{3+}, and Gd^{3+}) show great potential as MRI contrast agents due to their strong paramagnetic properties with high magnetic moments, which make Gd^{3+} suitable for T_1 MRI while other Ln^{3+} ions such as Tb, Dy, and Ho are suitable for T_2 MRI. These nanoparticles can be produced with customizable sizes, shapes, and surface modifications tailored for biomedical applications using various synthesis methods, such as hydrothermal, solvothermal, polyol, and thermal decomposition.

Larger nanoparticles exhibit higher r_2 values due to more intense magnetic interactions, although aggregation can reduce colloidal stability and relaxivity efficiency. In terms of shape, anisotropic nanoparticles, such as nanorods or rhombuses, demonstrate higher relaxivity values compared to spherical shapes due to more focused magnetic distribution. However, spherical shapes provide better colloidal stability, essential for preventing aggregation. Colloidal stability can also be improved through surface modification using polymers containing -COOH, -OH, or $-NH_2$ moieties conjugating with ligands targeting specific tumours, such as FA, HA, and RGD. Ligand conjugation on Gd_2O_3 nanoparticles enhances accumulation in tumour cells, enabling precise image-guided tumour therapy. For instance, cRGD/FA-PAA-Gd_2O_3 nanoparticles have shown superior contrast compared to nanoparticles with only a single targeting ligand. These nanoparticles also persist for longer in systemic circulation and have the potential to minimize the required contrast agent dose, thereby reducing side effects.

Innovations in this field also open opportunities to integrate therapy with diagnosis, such as PDT and PTT, as well as using nanoparticles for drug or gene delivery and magnetic hyperthermia-based therapy. With rapid advancements in lanthanide nanoparticle development, the future of theranostic applications combining diagnostic and therapeutic capabilities is becoming increasingly promising. Functionalized nanoparticles can be designed to serve dual roles as MRI contrast agents and carriers for chemotherapeutic drugs or genes, offering advantages in early detection and more targeted treatment. Furthermore, by minimizing side effects on normal cells and increasing tumour selectivity, nanoparticle technology could revolutionize cancer care, providing safer and more effective therapeutic alternatives. As research and development progress, lanthanide-based nanoparticles have the potential to become indispensable tools in the medical field, particularly in radiology-based cancer diagnosis and therapy. However, further research is important to optimize these nanoparticles for tumour-targeted diagnosis and therapy, along with rigorous toxicological assessments to ensure safety before clinical trials.

CRediT authorship contribution statement

Azmi Aulia Rahmani: Writing – original draft. **Qi Jia:** Writing – review & editing. **Husein H. Bahti:** Conceptualization. **Retna Putri Fauzia:** Writing – review & editing, Funding acquisition, Conceptualization. **Santhy Wyantuti:** Writing – review & editing, Funding acquisition, Conceptualization.

Declaration of competing interest

The authors declare that they have no known competing financial interests or personal relationships that could have appeared to influence the work reported in this paper.

Acknowledgments

The authors would like to acknowledge the financial support from Academic Leadership Grant and Review Article contract number [2274/UN6.3.1/PT.00/2024] of Padjadjaran University – Indonesia; Padjadjaran Academic Recharging 2023; and the Indonesian Ministry of Education and Culture, Indonesia [3993/UN6.3.1/PT.00/2024].

References

[1] M.Y. Ahmad, M.W. Ahmad, H. Yue, S.L. Ho, J.A. Park, K.H. Jung, H. Cha, S. Marasini, A. Ghazanfari, S. Liu, T. Tegafaw, In vivo positive magnetic resonance imaging applications of poly(methyl vinyl ether-alt-maleic acid)-coated ultra-small paramagnetic gadolinium oxide nanoparticles, Molecules. 25 (5) (2020) 1159, https://doi.org/10.3390/molecules25051159.

[2] D. González-Mancebo, A.I. Becerro, A. Corral, S. García-Embid, M. Balcerzyk, M.L. Garcia-Martin, J.M. de la Fuente, M. Ocaña, Design of a nanoprobe for high field magnetic resonance imaging, dual energy X-ray computed tomography and luminescent imaging, J. Colloid Interface Sci. 573 (2020) 278–286, https://doi.org/10.1016/j.jcis.2020.03.101.

[3] T. Tegafaw, S. Liu, M.Y. Ahmad, A.K.A.A. Saidi, D. Zhao, Y. Liu, S.W. Nam, Y. Chang, G.H. Lee, Magnetic nanoparticle-based high-performance positive and negative magnetic resonance imaging contrast agents, Pharmaceutics. 15 (6) (2023) 1745, https://doi.org/10.3390/pharmaceutics15061745.

[4] D. Ni, J. Zhang, W. Bu, C. Zhang, Z. Yao, H. Xing, J. Wang, F. Duan, Y. Liu, W. Fan, X. Feng, PEGylated NaHoF4 nanoparticles as contrast agents for both X-ray computed tomography and ultra-high field magnetic resonance imaging, Biomaterials 76 (2016) 218–225, https://doi.org/10.1016/j.biomaterials.2015.10.063.

[5] A. Fatima, M.W. Ahmad, A.K.A. Al Saidi, A. Choudhury, Y. Chang, G.H. Lee, Recent advances in gadolinium based contrast agents for bioimaging applications, Nanomaterials 11 (9) (2021) 2449, https://doi.org/10.3390/nano11092449.

[6] Z. Li, J. Guo, M. Zhang, G. Li, L. Hao, Gadolinium-coated mesoporous silica nanoparticle for magnetic resonance imaging, Front. Chem. 10 (2022) 1–10, https://doi.org/10.3389/fchem.2022.837032.

[7] S. Marasini, H. Yue, S.L. Ho, K.H. Jung, J.A. Park, H. Cha, A. Ghazanfari, M.Y. Ahmad, S. Liu, Y.J. Jang, X. Miao, D-glucuronic acid-coated ultrasmall paramagnetic Ln_2O_3 (Ln = Tb, Dy, and Ho) nanoparticles: magnetic properties, water proton relaxivities, and fluorescence properties, Eur. J. Inorg. Chem. 34 (2019) 3832–3839, https://doi.org/10.1002/ejic.201900378.

[8] X. Miao, W. Xu, H. Cha, Y. Chang, I.T. Oh, K.S. Chae, T. Tegafaw, S.L. Ho, S.J. Kim, G.H. Lee, Ultrasmall Gd_2O_3 nanoparticles surface-coated by polyacrylic acid (PAA) and their PAA-size dependent relaxometric properties, Appl. Surf. Sci. 477 (2019) 111–115, https://doi.org/10.1016/j.apsusc.2017.11.225.

[9] Caro, P.- B., M. Pernia Leal, and García-Martín, PEgylated terbium-based nanorods as multimodal bioimaging contrast agent, *ACS Appl. Nano Mater.*, 4(4), 4199–4207. https://doi.org/10.1021/acsanm.1c00569.

[10] X. Han, K. Xu, O. Taratula, K. Farsad, Applications of nanoparticles in biomedical imaging, Nanoscale 11 (3) (2019) 799–819, https://doi.org/10.1039/c8nr07769j.

[11] F. Whba, F. Mohamed, N.R.A. Md Rosli, I. Abdul Rahman, M.I. Idris, The crystalline structure of gadolinium oxide nanoparticles (Gd_2O_3-NPs) synthesized at different temperatures via X-ray diffraction (XRD) technique, Radiat. Phys. Chem. 179 (2021), https://doi.org/10.1016/j.radphyschem.2020.109212.

[12] Marasini, S., Yue, H., Ho, S.L., Cha, H., Park, J.A., Jung, K.H., Ghazanfari, A., Ahmad, M.Y., Liu, S., Chae, K.S. and Chang, Y., A novel paramagnetic nanoparticle T2 magnetic resonance imaging contrast agent with high colloidal stability: polyacrylic acid-coated ultrafine dysprosium oxide nanoparticles *Bull. Korean Chem. Soc.*,41(8), 829–839. https://doi.org/10.1002/bkcs.12074.

[13] J.G. Croissant, Y. Fatieiev, A. Almalik, N.M. Khashab, Mesoporous silica and organosilica nanoparticles: physical chemistry, biosafety, delivery strategies, and biomedical applications, Adv. Healthc. Mater. 7 (4) (2018), https://doi.org/10.1002/adhm.201700831.

[14] J. Yin, C. Li, D. Chen, J. Yang, H. Liu, W. Hu, Y. Shao, Structure and dysprosium dopant engineering of gadolinium oxide nanoparticles for enhanced dual-modal magnetic resonance and fluorescence imaging, Phys. Chem. Chem. Phys. 19 (7) (2017) 5366–5376, https://doi.org/10.1039/c6cp06712c.

[15] H. Yue, J.A. Park, S.L. Ho, M.Y. Ahmad, H. Cha, S. Liu, T. Tegafaw, S. Marasini, A. Ghazanfari, S. Kim, K.S. Chae, New class of efficient t2 magnetic resonance imaging contrast agent: carbon-coated paramagnetic dysprosium oxide nanoparticles, Pharmaceuticals 13 (10) (2020), https://doi.org/10.3390/ph13100312.

[16] P. Zhang, Y. Li, W. Tang, J. Zhao, L. Jing, K.J. McHugh, Theranostic nanoparticles with disease-specific administration strategies, Nano Today 42 (2022), https://doi.org/10.1016/j.nantod.2021.101335. Elsevier B.V.Feb. 01,.

[17] X. Zhang, B. Blasiak, A.J. Marenco, S. Trudel, B. Tomanek, F.C. van Veggel, Design and regulation of $NaHoF_4$ and $NaDyF_4$ nanoparticles for high-field magnetic resonance imaging, Chem. Mater. 28 (9) (2016) 3060–3072, https://doi.org/10.1021/acs.chemmater.6b00264. May.

[18] M. Difonzo, L. Fliedel, N. Mignet, K. Andrieux, K. Alhareth, How could nanomedicine improve the safety of contrast agents for MRI during pregnancy? Sci. 4 (1) (2022) 11, https://doi.org/10.3390/sci4010011.

[19] T. Gayathri, N.M. Sundaram, R.A. Kumar, Gadolinium oxide nanoparticles for magnetic resonance imaging and cancer theranostics, J. Bionanosci. 9 (6) (2015) 409–423, https://doi.org/10.1166/jbns.2015.1325.

[20] S.D. Serai, M.L. Ho, M. Artunduaga, S.S. Chan, G.B. Chavhan, Components of a magnetic resonance imaging system and their relationship to safety and image quality, Pediatr. Radiol. 51 (5) (2021) 716–723, https://doi.org/10.1007/s00247-020-04894-9.

[21] N.J. Serkova, Nanoparticle-based magnetic resonance imaging on tumor-associated macrophages and inflammation, Front. Immunol. 8 (2017) 590, https://doi.org/10.3389/fimmu.2017.00590.

[22] M. Norek, G.A. Pereira, C.F. Geraldes, A. Denkova, W. Zhou, J.A. Peters, NMR transversal relaxivity of suspensions of lanthanide oxide nanoparticles, J. Phys. Chem. C 111 (28) (2007) 10240–10246, https://doi.org/10.1021/jp072288l.

[23] F. Chen, M. Chen, C. Yang, J. Liu, N. Luo, G. Yang, D. Chen, L. Li, Terbium-doped gadolinium oxide nanoparticles prepared by laser ablation in liquid for use as fluorescence and magnetic resonance imaging dual-modal contrast agents, Phys. Chem. Chem. Phys. 17 (2) (2015) 1189–1196, https://doi.org/10.1039/C4CP04380D.

[24] S. Lacerda, Targeted contrast agents for molecular MRI, Inorganics 6 (4) (2018) 1–17, https://doi.org/10.3390/inorganics6040129.

[25] M. Jeon, M.V. Halbert, Z.R. Stephen, M. Zhang, Iron oxide nanoparticles as T1 contrast agents for magnetic resonance imaging: fundamentals, challenges, applications, and prospectives, Adv. Mater. 33 (23) (2021) 1906539, https://doi.org/10.1002/adma.201906539.

[26] B. Babić-Stojić, V. Jokanović, D. Milivojević, M. Požek, Z. Jagličić, D. Makovec, K. Arsikin, V. Paunović, Gd_2O_3 nanoparticles stabilized by hydrothermally modi fi ed dextrose for positive contrast magnetic resonance imaging, J. Magn. Magn. Mater. 403 (2016) 118–126, https://doi.org/10.1016/j.jmmm.2015.11.075.

[27] M.A. Chowdhury, M etal-organic-frameworks for biomedical applications in drug delivery, and as MRI contrast agents, J. Biomed. Mater. Res. Part A 105 (4) (2017) 1184–1194, https://doi.org/10.1002/jbm.a.35995, 2016.

[28] T. T Mortezazadeh, E. Gholibegloo, M. Khoobi, N.R. Alam, S. Haghgoo, A. Mesbahi, In vitro and in vivo characteristics of doxorubicin-loaded cyclodextrine-based polyester modified gadolinium oxide nanoparticles: a versatile targeted theranostic system for tumour chemotherapy and molecular resonance imaging, J. Drug Target. 28 (5) (2020) 533–546, https://doi.org/10.1080/1061186X.2019.1703188.

[29] N. Kostevšek, A review on the optimal design of magnetic nanoparticle-based T_2 MRI contrast agents, Magnetochemistry 6 (1) (2020) 1–12, https://doi.org/10.3390/magnetochemistry6010011.

[30] M. Salehipour, S. Rezaei, J. Mosafer, Z. Pakdin-Parizi, A. Motaharian, M. Mogharabi-Manzari, Recent advances in polymer-coated iron oxide nanoparticles as magnetic resonance imaging contrast agents, J. Nanoparticle Res. 23 (2021) 1–35, https://doi.org/10.1007/s11051-021-05156-x.

[31] D. González-Mancebo, A.I. Becerro, T.C. Rojas, M.L. García-Martín, J.M. de la Fuente, M. Ocaña, HoF_3 and DyF_3 nanoparticles as contrast agents for high-field magnetic resonance imaging, Art. Particle Syst. Characteriz. 34 (10) (2017) 1700116, https://doi.org/10.1002/ppsc.201700116.

[32] S. Marasini, H. Yue, S.L. Ho, J.A. Park, S. Kim, K.H. Jung, H. Cha, S. Liu, T. Tegafaw, M.Y. Ahmad, A. Ghazanfari, Synthesis, characterizations, and 9.4 tesla t2 mr images of polyacrylic acid-coated terbium(iii) and holmium(iii) oxide nanoparticles, Nanomaterials 11 (5) (2021) 1355, https://doi.org/10.3390/nano11051355.

[33] S. Liu, H. Yue, S.L. Ho, S. Kim, J.A. Park, T. Tegafaw, M.Y. Ahmad, S. Kim, A.K.A.A. Saidi, D. Zhao, Y. Liu, Polyethylenimine-coated ultrasmall holmium oxide nanoparticles: synthesis, characterization, cytotoxicities, and water proton spin relaxivities, Nanomaterials 12 (9) (2022) 1588, https://doi.org/10.3390/nano12091588.

[34] A. Escudero, A.I. Becerro, C. Carrillo-Carrión, N.O. Nunez, M.V. Zyuzin, M. Laguna, D. González-Mancebo, M. Ocaña, W.J. Parak, Rare earth based nanostructured materials: synthesis, functionalization, properties and bioimaging and biosensing applications, Nanophotonics 6 (5) (2017) 881–921, https://doi.org/10.1515/nanoph-2017-0007.

[35] Y.X.G.A.H. Jayatissa, Z. Yu, X. Chen, M. Li, Hydrothermal synthesis of nanomaterials, Nanometer (2020) 8917013.

[36] N. Abid, A.M. Khan, S. Shujait, K. Chaudhary, M. Ikram, M. Imran, J. Haider, M. Khan, Q. Khan, M. Maqbool, Synthesis of nanomaterials using various top-down and bottom-up approaches, influencing factors, advantages, and disadvantages: a review, Adv. Colloid. Interface Sci. 300 (2022) 102597, https://doi.org/10.1016/j.cis.2021.102597.

[37] A.M. Famia, M. Muldarisnur, Pengaruh temperatur sintesis hidrotermal terhadap diameter nanopartikel seng oksida, J. Fis. Unand. 8 (2) (2019) 127–132, https://doi.org/10.25077/jfu.8.2.127-132.2019.

[38] S. Wyantuti, B. Fadhilatunnisa, R.P. Fauzia, J.I.A. Qi, A.A. Rahmani, H.H. Bahti, Response surface methodology box-behnken design to optimise the hydrothermal synthesis of gadolinium nanoparticles, Chinese J. Anal. Chem. 51 (10) (2023) 100316, https://doi.org/10.1016/j.cjac.2023.100316.

[39] S. Hazarika, N. Paul, D. Mohanta, Rapid hydrothermal route to synthesize cubic-phase gadolinium oxide nanorods, Bull. Mater. Sci. 37 (2014) 789–796.

[40] S. Hazarika, P.S. Behera, D. Mohanta, R. Nirmala, Magnetocaloric effect of Gd_2O_3 nanorods with 5 % Eu-substitution, Appl. Surf. Sci. 491 (2019) 779–783, https://doi.org/10.1016/j.apsusc.2019.05.266.

[41] S.M. ul Hassan, M.T. Siddique, M. Fakhar-e-Alam, M. Atif, A. Saifullah, N. Marwat, A. Khurshid, O. Noor, N. Hossain, S. Ahmad, K.S. Alimgeer, Hydrothermally synthesized lanthanide-incorporated multifunctional zirconia nanoparticles: potential candidate for multimodal imaging, *J. King Saud Univ. - Sci.* 34 (5) (2022) 102080, https://doi.org/10.1016/j.jksus.2022.102080.

[42] C. Wu, R. Cai, T. Zhao, L. Wu, L. Zhang, J. Jin, L. Xu, P. Li, T. Li, M. Zhang, F. Du, Hyaluronic acid-functionalized gadolinium oxide nanoparticles for magnetic resonance imaging-guided radiotherapy of tumors, Nanoscale Res. Lett. 15 (2020) 1–12, https://doi.org/10.1186/s11671-020-03318-9.

[43] H.J. Cho, Recent progresses in the development of hyaluronic acid-based nanosystems for tumor-targeted drug delivery and cancer imaging, J. Pharm. Invest. 50 (2) (2020) 115–129, https://doi.org/10.1007/s40005-019-00448-w.

[44] S. Yin, S. Akita, M. Shinozaki, R. Li, T. Sato, Synthesis and morphological control of rare earth oxide nanoparticles by solvothermal reaction, J. Mater. Sci. 43 (7) (2008) 2234–2239, https://doi.org/10.1007/s10853-007-2070-3.

[45] A. Dougherty, E.L. Nasution, F. Iskandar, G. Dougherty, Facile solvothermal synthesis and functionalization of polyethylene glycol-coated paramagnetic $Gd_2(CO_3)_3$ particles and corresponding Gd_2O_3 nanoparticles for use as MRI contrast agents, J. Sci. Adv. Mater. Dev. 4 (1) (2019) 72–79, https://doi.org/10.1016/j.jsamd.2018.12.005. Mar. 2019.

[46] T. Zhang, M. Deng, L. Zhang, Z. Liu, Y. Liu, S. Song, T. Gong, Q. Yuan, Facile synthesis of holmium-based nanoparticles as a CT and MRI dual-modal imaging for cancer diagnosis, Front. Oncol. 11 (2021) 741383, https://doi.org/10.3389/fonc.2021.741383.

[47] Y.J. Jang, S. Liu, H. Yue, J.A. Park, H. Cha, S.L. Ho, S. Marasini, A. Ghazanfari, M.Y. Ahmad, X. Miao, T. Tegafaw, Hydrophilic biocompatible poly(Acrylic acid-co-maleic acid) polymer as a surface-coating ligand of ultrasmall Gd_2O_3 nanoparticles to obtain a high r_1 value and T_1 Mr images, Diagnostics 11 (1) (2021) 2, https://doi.org/10.3390/diagnostics11010002.

[48] T.S. Atabaev, J.H. Lee, D.W. Han, K.S. Choo, U.B. Jeon, J.Y. Hwang, J.A. Yeom, C. Kang, H.K. Kim, Y.H. Hwang, Multicolor nanoprobes based on silica-coated gadolinium oxide nanoparticles with highly reduced toxicity, RSC. Adv. 6 (24) (2016) 19758–19762, https://doi.org/10.1039/C5RA27685C.

[49] A.K. Khan, R. Rashid, G. Murtaza, A.J.T.R. Zahra, Gold nanoparticles : synthesis and applications in drug, Trop. J. Pharm. Res. 13 (7) (2014) 1169–1177, https://doi.org/10.4314/tjpr.v13i7.23.

[50] A. Saha, S.C. Mohanta, K. Deka, P. Deb, P.S. Devi, Surface-engineered multifunctional Eu : Gd_2O_3 nanoplates for targeted and pH-responsive drug delivery and imaging applications, ACS. Appl. Mater. Interfaces 9 (4) (2017) 4126–4141, https://doi.org/10.1021/acsami.6b12804.

[51] N. Babayevska, P. Florczak, M. Woźniak-Budych, M. Jarek, G. Nowaczyk, T. Zalewski, S. Jurga, Applied surface science functionalized multimodal ZnO@Gd_2O_3 nanosystems to use as perspective contrast agent for MRI, Appl. Surf. Sci. 404 (2017) 129–137, https://doi.org/10.1016/j.apsusc.2017.01.274.

[52] W. Cai, Y. Zhang, J. Wang, Z. Wang, Y. Tian, H. Liu, H. Pan, L. Fu, W. Chen, C. Wu, X. Wang, Engineering the surface of Gd_2O_3 nanoplates for improved T1-weighted magnetic resonance imaging, Chem. Eng. J. 380 (2020) 122473, https://doi.org/10.1016/j.cej.2019.122473.

[53] S.L. Ho, G. Choi, H. Yue, H.K. Kim, K.H. Jung, J.A. Park, M.H. Kim, Y.J. Lee, J.Y. Kim, X. Miao, M.Y. Ahmad, In vivo neutron capture therapy of cancer using ultrasmall gadolinium oxide nanoparticles with cancer-targeting ability, RSC. Adv. 10 (2) (2019) 865–874, https://doi.org/10.1039/c9ra08961f.

[54] E. Gómez-González, N.O. Núñez, C. Caro, M.L. Garcia-Martín, M. Ocaña, Carboxylate functionalized $NaDy(MoO_4)_2$ nanoparticles with tunable size and shape as high magnetic field MRI contrast agents, J. Colloid Interface Sci. 629 (2023) 310–321, https://doi.org/10.1016/j.jcis.2022.08.130.

[55] A. Guleria, P. Pranjali, M.K. Meher, A. Chaturvedi, S. Chakraborti, R. Raj, K.M. Poluri, D. Kumar, Effect of polyol chain length on proton relaxivity of gadolinium oxide nanoparticles for enhanced magnetic resonance imaging contrast, J. Phys. Chem. C 123 (99) (2019) 18061–18070, https://doi.org/10.1021/acs.jpcc.9b04089.

[56] K. Kattel, J.Y. Park, W. Xu, H.G. Kim, E.J. Lee, B.A. Bony, W.C. Heo, S. Jin, J.S. Baeck, Y. Chang, T.J. Kim, Paramagnetic dysprosium oxide nanoparticles and dysprosium hydroxide nanorods as T_2 MRI contrast agents, Biomaterials 33 (11) (2012) 3254–3261, https://doi.org/10.1016/j.biomaterials.2012.01.008.

[57] T.S. Atabaev, Y.C. Shin, S.J. Song, D.W. Han, N.H. Hong, Toxicity and t_2-weighted magnetic resonance imaging potentials of holmium oxide nanoparticles, Nanomaterials 7 (8) (2017) 216, https://doi.org/10.3390/nano7080216.

[58] E. Gómez-González, C. Caro, D. Martínez-Gutiérrez, M.L. García-Martín, M. Ocaña, A.I. Becerro, Holmium phosphate nanoparticles as negative contrast agents for high-field magnetic resonance imaging: synthesis, magnetic relaxivity study and in vivo evaluation, J. Colloid Interface Sci. 587 (2021) 131–140, https://doi.org/10.1016/j.jcis.2020.11.119.

[59] J. Zhang, Z. Lin, M. Zhao, W. Xu, F. Nian, Preparation and MRI performances of core-shell structural PEG salicylic acid-gadolinium composite nanoparticles, J. Rare Earths 40 (7) (2022) 1098–1105, https://doi.org/10.1016/j.jre.2021.09.006.

[60] D. Chauhan, R. Kumar, A.K. Panda, P.R. Solanki, An efficient electrochemical biosensor for Vitamin-D3 detection based on aspartic acid functionalized gadolinium oxide nanorods, J. Mater. Res. Technol. 8 (6) (2019) 5490–5503, https://doi.org/10.1016/j.jmrt.2019.09.017.

[61] E. Gómez-Gónzalez, N.O. Núñez, C. Caro, M.L. García-Martín, Y. Fernández-Afonso, J.M. de la Fuente, M. Balcerzyk, M. Ocaña, Dysprosium and holmium vanadate nanoprobes as high-performance contrast agents for high-field magnetic resonance and computed tomography imaging, Inorg. Chem. 60 (1) (2021) 152–160, https://doi.org/10.1021/acs.inorgchem.0c02601.

[62] E. Gholibegloo, T. Mortezazadeh, F. Salehian, H. Forootanfar, L. Firoozpour, A. Foroumadi, A. Ramazani, M. Khoobi, Folic acid decorated magnetic nanosponge: an efficient nanosystem for targeted curcumin delivery and magnetic resonance imaging, J. Colloid Interface Sci 556 (2019) 128–139, https://doi.org/10.1016/j.jcis.2019.08.046.

[63] D.J. Pochapski, C. Carvalho dos Santos, G.W. Leite, S.H. Pulcinelli, C.V. Santilli, Zeta potential and colloidal stability predictions for inorganic nanoparticle dispersions: eff ects of experimental conditions and electrokinetic models on the interpretation of results, Langmuir 37 (45) (2021) 13379–13389, https://doi.org/10.1021/acs.langmuir.1c02056.

[64] Prakash, S., Mishra, R., Malviya, R. and Sharma, P.K., Measurement techniques and pharmaceutical applications of zeta potential : a Review, *J. Chronother. Drug Deliv.*, 5(2), pp.33–40.

[65] V. Gupta, P. Trivedi, In vitro *and* in vivo *characterization of pharmaceutical topical nanocarriers containing anticancer drugs for skin cancer treatment.* Lipid Nanocarriers For Drug Targeting, William Andrew Publishing, 2018, pp. 563–627, https://doi.org/10.1016/B978-0-12-813687-4.00015-3.

[66] T. Mortezazadeh, E. Gholibegloo, N.R. Alam, S. Dehghani, S. Haghgoo, H. Ghanaati, M. Khoobi, Gadolinium (III) oxide nanoparticles coated with folic acid functionalized poly (β cyclodextrin-copentetic acid) as a biocompatible targeted nano contrast agent for cancer diagnostic : in vitro and in vivo studies, Magn. Resonan. Mater. Phys., Biol. Med. 32 (4) (2019) 487–500, https://doi.org/10.1007/s10334-019-00738-2.

[67] X. Zheng, Y. Wang, L. Sun, N. Chen, L. Li, S. Shi, S. Malaisamy, C. Yan, TbF_3 nanoparticles as dual-mode contrast agents for ultrahigh field magnetic resonance imaging and X-ray computed tomography, Nano Res. 9 (4) (2016) 1135–1147, https://doi.org/10.1007/s12274-016-1008-y. Apr. 2016.

[68] S. Marasini, H. Yue, A. Ghazanfari, S.L. Ho, J.A. Park, S. Kim, H. Cha, S. Liu, T. Tegafaw, M.Y. Ahmad, A.K.A.A. Saidi, Polyaspartic acid-coated paramagnetic gadolinium oxide nanoparticles as a dual-modal T_1 and T_2 magnetic resonance imaging contrast agent, Appl. Sci. 11 (17) (2021) 8222, https://doi.org/10.3390/app11178222.

[69] N.R. Chawda, S.K. Mahapatra, I. Banerjee, Surface-engineered gadolinium oxide nanorods and nanocuboids for bioimaging, Rare Metals. 40 (2020) 848–857, https://doi.org/10.1007/s12598-020-01378-5.

[70] M.J. Akhtar, M. Ahamed, H. Alhadlaq, Gadolinium oxide nanoparticles induce toxicity in human endothelial huvecs via lipid peroxidation, mitochondrial dysfunction, Nanomaterials 10 (9) (2020) 1–18, https://doi.org/10.3390/nano10091675.

[71] H. Setiawan, F. Triyatna, A. Nurmanjaya, M. Subechi, D.A. Sarwono, A.A. Billah, F. Rindiyantono, Synthesis and characterization of gadolinium nanoparticles using polyol method as a candidate for MRI contrast agent synthesis and characterization of gadolinium nanoparticles using polyol method as a candidate for MRI contrast agent, J. Physics: Conference Series 2193 (1) (2022) 012010, https://doi.org/10.1088/1742-6596/2193/1/012010.

[72] S. Marasini, H. Yue, A. Ghazanfari, S.L. Ho, J.A. Park, S. Kim, H. Cha, S. Liu, T. Tegafaw, M.Y. Ahmad, A.K.A.A. Saidi, Polyaspartic acid-coated paramagnetic gadolinium oxide nanoparticles as a dual-modal t1 and t2 magnetic resonance imaging contrast agent, Appl. Sci. 11 (17) (2021) 8222, https://doi.org/10.3390/app11178222.

[73] J. Wahsner, E.M. Gale, A. Rodríguez-Rodríguez, P. Caravan, Chemistry of MRI contrast agents: current challenges and new frontiers, Chem. Rev. 119 (2) (2019) 957–1057, https://doi.org/10.1021/acs.chemrev.8b00363.

[74] A.D. Sherry, P. Caravan, R.E. Lenkinski, Primer on gadolinium chemistry, J. Magn. Resonan. Imag. 30 (6) (2009) 1240–1248, https://doi.org/10.1002/jmri.21966.

[75] P. Caravan, J.J. Ellison, T.J. McMurry, R.B. Lauffer, Gadolinium(III) chelates as MRI contrast agents: structure, dynamics, and applications, Chem. Rev. 99 (9) (1999) 2293–2352, https://doi.org/10.1021/cr980440x.

[76] M. Norek, E. Kampert, U. Zeitler, J.A. Peters, Tuning of the size of Dy_2O_3 nanoparticles for optimal performance as an MRI contrast agent, J. Am. Chem. Soc. 130 (15) (2008) 5335–5340, https://doi.org/10.1021/ja711492y.

[77] F. Hajesmaeelzadeh, S. Shanehsazzadeh, C. Grüttner, F.J. Daha, M.A. Oghabian, Effect of coating thickness of iron oxide nanoparticles on their relaxivity in the MRI, Iran. J. Basic Med. Sci. 19 (2) (2016) 166–171, 27081461.

[78] A. Jain, P.G. Fournier, V. Mendoza-Lavaniegos, P. Sengar, F.M. Guerra-Olvera, E. Iñiguez, T.G. Kretzschmar, G.A. Hirata, P. Juárez, Functionalized rare earth-doped nanoparticles for breast cancer nanodiagnostic using fluorescence and CT imaging, J. Nanobiotechnol. 16 (1) (2018) 1–18, https://doi.org/10.1186/s12951-018-0359-9.

[79] T. Feczkó, A. Piiper, T. Pleli, C. Schmithals, D. Denk, S. Hehlgans, F. Rödel, T.J. Vogl, M.G. Wacker, Theranostic sorafenib-loaded polymeric nanocarriers manufactured by enhanced gadolinium conjugation techniques, Pharmaceutics 11 (10) (2019) 489, https://doi.org/10.3390/pharmaceutics11100489.

[80] Y. Shi, R. van der Meel, X. Chen, T. Lammers, The EPR effect and beyond: strategies to improve tumor targeting and cancer nanomedicine treatment efficacy, Theranostics 10 (17) (2020) 7921–7924, https://doi.org/10.7150/thno.49577.

[81] M. Abbasi, M. Sohail, M.U. Minhas, A. Mahmood, S.A. Shah, A. Munir, International journal of biological macromolecules folic acid-decorated alginate nanoparticles loaded hydrogel for the oral delivery of diferourylmethane in colorectal cancer, Int. J. Biol. Macromol. 233 (2023) 123585, https://doi.org/10.1016/j.ijbiomac.2023.123585.

[82] L. Smith, H.L. Byrne, D. Waddington, Z. Kuncic, Nanoparticles for MRI guided radiation therapy : a review, Cancer Nanotechnol. 13 (1) (2022) 1–28, https://doi.org/10.1186/s12645-022-00145-8.

[83] S.L. Ho, H. Yue, S. Lee, T. Tegafaw, M.Y. Ahmad, S. Liu, A.K.A.A. Saidi, D. Zhao, Y. Liu, S.W. Nam, K.S. Chae, Mono and multiple tumor-targeting ligand-coated ultrasmall gadolinium oxide nanoparticles: enhanced tumor imaging and blood circulation, Pharmaceutics 14 (7) (2022) 1458, https://doi.org/10.3390/pharmaceutics14071458.

[84] N. Babayevska, et al., Functionalized multimodal ZnO@Gd 2 O 3 nanosystems to use as perspective contrast agent for MRI, Appl. Surf. Sci. 404 (2017) 129–137, https://doi.org/10.1016/j.apsusc.2017.01.274. May.

[85] R.P. Fauzia, H.H. Bahti, Sintesis dan karakterisasi (3-aminopropil)-trimetoksisilan terkonjugasi asam folat untuk fungsionalisasi nanopartikel, Chim. Natura Acta 11 (1) (2023) 36–40, https://doi.org/10.24198/cna.v11.n1.45884.

[86] Y. Zhao, C. Cui, J. Zhan, G. Xuan, Study of folate receptor-targeted macromolecular gadolinium complex tumor contrast agent, Mater. Today Commun. 33 (2022) 104988, https://doi.org/10.1016/j.mtcomm.2022.104988.

[87] T.E. Kim, H.J. Jang, S.W. Park, J. Wei, S. Cho, W.I. Park, B.R. Lee, C.D. Yang, Y.K. Jung, Folic acid functionalized carbon dot /polypyrrole nanoparticles for specifc bioimaging and photothermal therapy, ACS Appl. Bio Mater. 4 (4) (2021) 3453–3461, https://doi.org/10.1021/acsabm.1c00018.

[88] P.V. Pawar, A.J. Domb, N. Kumar, *Systemic targeting systems-EPR effect, ligand targeting systems*. Focal Controlled Drug Delivery, 2014, pp. 61–91, https://doi.org/10.1007/978-1-4614-9434-8_3.

[89] E. Allard-Vannier, K. Hervé-Aubert, K. Kaaki, T. Blondy, A. Shebanova, K.V. Shaitan, A.A. Ignatova, M.L. Saboungi, A.V. Feofanov, I. Chourpa, Folic acid-capped PEGylated magnetic nanoparticles enter cancer cells mostly via clathrin-dependent endocytosis, Biochim. Biophys. Acta (BBA)-Gen. Subj. 1861 (6) (2019) 1578–1586, https://doi.org/10.1016/j.bbagen.2016.11.045.

[90] M. Rohrer, H. Bauer, J. Mintorovitch, M. Requardt, H.J. Weinmann, Comparison of magnetic properties of MRI contrast media solutions at different magnetic field strengths, Invest. Radiol. 40 (11) (2005) 715–724, https://doi.org/10.1097/01.rli.0000184756.66360.d3.

[91] D. González-Mancebo, A.I. Becerro, C. Caro, E. Gómez-González, M.L. García-Martín, M. Ocaña, Nanoparticulated bimodal contrast agent for ultra-high-field magnetic resonance imaging and spectral x-ray computed tomography, Inorg. Chem. 63 (23) (2024) 10648–10656, https://doi.org/10.1021/acs.inorgchem.4c01114.

[92] I. Khan, K. Saeed, I. Khan, Nanoparticles: properties, applications and toxicities, Arab. J. Chem. 12 (7) (2019) 908–931, https://doi.org/10.1016/j.arabjc.2017.05.011.

[93] M.K. Hossain, M.I. Khan, A. El-Denglawey, A review on biomedical applications, prospects, and challenges of rare earth oxides, Appl. Mater. Today 24 (2021) 101104, https://doi.org/10.1016/j.apmt.2021.101104.

[94] V. Sanna, N. Pala, M. Sechi, Targeted therapy using nanotechnology: focus on cancer, Int. J. Nanomed. 9 (1) (2014) 467–483, https://doi.org/10.2147/IJN.S36654, 2014.

[95] Y. Liu, N. Zhang, Gadolinium loaded nanoparticles in theranostic magnetic resonance imaging, Biomaterials 33 (21) (2012) 5363–5375, https://doi.org/10.1016/j.biomaterials.2012.03.084.

[96] L. Zhang, Z. Yang, J. Ren, L. Ba, W. He, C.Y. Wong, Multifunctional oxygen-enriching nano-theranostics for cancer- specific magnetic resonance imaging and enhanced photodynamic /photothermal therapy, Nano Res. 13 (5) (2020) 1389–1398, https://doi.org/10.1007/s12274-020-2646-7.

[97] X. Yang, Y. Wang, X. Shen, C. Su, J. Yang, M. Piao, F. Jia, G. Gao, L. Zhang, Q. Lin, One-step synthesis of photoluminescent carbon dots with excitation-independent emission for selective bioimaging and gene delivery, J. Colloid. Interface Sci. 492 (2017) 1–7, https://doi.org/10.1016/j.jcis.2016.12.057.

[98] B. Wang, W. Lin, Z. Mao, C Gao, Near-infrared light triggered photothermal therapy and enhanced photodynamic therapy with a tumor-targeting hydrogen peroxide shuttle, J. Mater. Chem. B 6 (19) (2018) 3145–3155, https://doi.org/10.1039/C8TB00476E.

[99] W. Chen, J. Zhao, M. Hou, M. Yang, C. Yi, Gadolinium-porphyrin based polymer nanotheranostics for fluorescence/magnetic resonance imaging guided photodynamic therapy, Nanoscale 13 (38) (2021) 16197–16206, https://doi.org/10.1039/d1nr04489c.

[100] P.S. Jiang, H.Y. Tsai, P. Drake, F.N. Wang, C.S. Chiang, Gadolinium-doped iron oxide nanoparticles induced magnetic field hyperthermia combined with radiotherapy increases tumour response by vascular disruption and improved oxygenation, Int. J. Hyperther. 33 (7) (2017) 770–778, https://doi.org/10.1080/02656736.2017.1308019.

[101] R. Zhang, M. Liu, S. Liu, X. Liang, R. Lu, X. Shuai, D. Wu, Z. Cao, Acta biomaterialia holmium (III)-doped multifunctional nanotheranostic agent for ultra-high-field magnetic resonance imaging-guided chemo-photothermal tumor therapy, Acta Biomater. 172 (2023) 454–465, https://doi.org/10.1016/j.actbio.2023.10.017.

[102] J.H. Jin, H. Um, J.H. Oh, Y. Huh, Y. Jung, D. Kim, Gadolinium silicate-coated porous silicon nanoparticles as an MRI contrast agent and drug delivery carrier, Mater. Chem. Phys. 287 (2022) 126345, https://doi.org/10.1016/j.matchemphys.2022.126345.

[103] A. Nasrolahi Shirazi, M.I. Sajid, D. Mandal, D. Stickley, S. Nagasawa, J. Long, S. Lohan, K. Parang, R.K. Tiwari, Cyclic peptide-gadolinium nanocomplexes as sirna delivery tools, Pharmaceuticals 14 (11) (2021) 1–16, https://doi.org/10.3390/ph14111064.